AUTOMATIC EDUCTION AND STATISTICAL ANALYSIS OF COHERENT STRUCTURES IN THE WALL REGION OF A CONFINED PLANE TURBULENT IMPINGING JET

M. Pavageau [(*)], K. Loubière, S. Gupta

GEPEA UMR 6144 - CNRS

Ecole des Mines de Nantes, Département Systèmes Energétiques et Environnement,

4 rue Alfred Kastler, BP 20722, 44307 Nantes Cedex 3, FRANCE

[(*)] Corresponding author:

Tel: 33-(0)2 51 85 82 67 / Fax: 33-(0)2 51 85 82 99 / Email: pavageau@emn.fr

---

Revised version – March 2006

Submitted for publication in
Experiments in fluids

Abstract

This paper describes a vortex detection algorithm used to expose and statistically characterize the coherent flow patterns observable in the velocity vector fields measured by Particle Image Velocimetry (PIV) in the impingement region of air curtains. The philosophy and the architecture of this algorithm are presented. Its strengths and weaknesses are discussed. The results of a parametrical analysis performed to assess the variability of the response of our algorithm to the 3 user-specified parameters in our eduction scheme are reviewed. The technique is illustrated in the case of a plane turbulent impinging twin-jet with an opening ratio of 10. The corresponding jet Reynolds number, based on the initial mean flow velocity U_0 and the jet width e, is 14000. The results of a statistical analysis of the size, shape, spatial distribution and energetic content of the coherent eddy structures detected in the impingement region of this test flow are provided. Although many questions remain open, new insights into the way these structures might form, organize and evolve are given. Relevant results provide an original picture of the plane turbulent impinging jet.

1. Introduction

Air curtains are separation devices based on the discharge of a plane air stream to isolate from each other two adjacent volumes with different climatic characteristics (in the broad sense of the term). The jet system, which may consist of one or several parallel air streams, provides a fluidic seal against heat, moisture and/or mass transfers between the separated areas without holding up the traffic of people, vehicles, materials or objects. Thus, air curtains are particularly useful in situations where conventional physical barriers are unacceptable for practical, technical, economic or safety reasons. The applications for air curtains are many. They include, but are not limited to, air conditioned areas, commercial entrances, refrigerated counters, clean rooms, testing chamber apparatus (e.g. thermal shock test chambers), industrial oven openings, tunnel fire safety systems, process line partitioning in the food or microelectronics industry, etc. (See Gupta 2005 and references therein).

The sealing efficiency of an air curtain is directly related to the amount of ambient fluid ingested into the main flow and carried across it by convection and diffusion. In this respect, it is obvious that the Kelvin-Helmoltz instabilities that develop in the shear layers along the lateral boundaries of the primary jet flow play a relevant role. However, the LES simulations of Beaubert and Viazzo (2003) have shown that mass transfers across the jet stream preferentially occur in the impingement region. This seems to be strongly related to the presence of large-scale organised motions in the form of elongated roll cells whose main axis is roughly perpendicular to the jet plane. Also detected experimentally by Yokobori et al. (1977), Sakakibara et al. (1997) and Maurel et al. (2004), these tubular structures are accelerated and stretched longitudinally by the wall flows developing on either side of the jet after impingement. It has been shown that they are characterized locally by a strong vortical intensity and a noticeable energetic content. Although this was much debated by Lyell and Huerre (1985) and Sakakibara et al. (1997), these roll cells often continue to be associated with Görtler type vortices that are due to streamline curvature near impingement.

Consequently, in place of or in addition to a passive or active control of the growth of the instabilities developing in the lateral mixing layers of a jet (Zaman and Hussain 1981 and references therein, Hsiao and Huang 1994, Vandsburger and Ding 1995, Rajagopalan and Ko 1996, Rajagopalan and Antonia 1998), the flow structure in the impingement region could be acted upon to improve the efficiency of air curtains. However, before working out appropriate solutions, it is necessary to better understand the way in which the large-scale structures present in the

impingement region of a jet form, evolve and contribute to transfer mechanisms. This is one of the objectives of our current research program as presented in this paper.

Our work has led to the development of an algorithm to automate the identification of vortical patterns embedded in instantaneous velocity vector maps obtained by standard Particle Image Velocimetry (PIV). The algorithm is designed to detect and characterize traces left by structures with their axis out of the measurement plane. The detection scheme is based on the assumption that a vortex centre is associated with a local pressure minimum. Structures are characterized topologically and energetically. As our PIV measurements are not time resolved, analysis is performed on series of instantaneous velocity fields and relevant results are reported mainly in the form of probability density functions (pdf) of the observed quantities.

The paper is organised as follows. Section 2 outlines the successive stages of the eduction scheme used in this work. It is followed by information and experimental details about the test case chosen here for illustration. The response of our eduction scheme to the user choices imposed by our approach is then discussed prior to the final presentation of the results obtained after application of our algorithm on 2D PIV velocity vector maps recorded in 5 measurement planes of the jet flow considered here for demonstration purposes. Like in Agrawal and Prasad (2002a), the results include probability density functions of vortex populations according to mean diameter, eccentricity, circulation, and vortical intensity, plotted here as a function of measurement plane position. In addition, cross probability density functions as a function of structure mean diameter and information about the spatial distribution of the detected structures are provided. Finally, conclusions and perspectives are given.

2. Automatic method for coherent structure eduction and characterization

We shall often use the term "coherent structure" to refer to the swirling motions detected by the method described below. We are aware that this may seem inappropriate for at least two reasons. First, although no consensual and general definition of a coherent structure has been established, it is agreed that structures said to be coherent should exhibit a certain degree of integrity over certain spatial and temporal scales (Hussain 1986, Robinson et al. 1989, Lesieur 1990, Robinson 1991). However, the technique presented in this paper does not necessarily allow the assessment of the spatial integrity of the detected structures during motion. It only allows it if it is applied to successive instantaneous velocity vector fields separated by a time step sufficiently lower than the coherence time (or life time) of these structures. Second, the consensus about coherent structures

puts forward spatial and temporal integrity scales that should be significantly larger than the smallest local turbulence scales. The point here is that our method can detect swirling patterns in any 2D velocity vector field, regardless of the actual size of the experimental observation window in physical space. As to whether the detected patterns can be classed as coherent structures, this necessarily requires some a priori knowledge of the flow under investigation.

2.1 Preliminary calculations (step 1)

2.1.1 Homogeneous filtering

Structure identification methods require the computation of spatial derivatives of fluid velocity. Therefore, a certain continuity and smoothness of the analysed velocity fields must be ensured. However, PIV measurements are discrete in space, with a spatial resolution usually much lower than what can be achieved numerically. They also contain a certain amount of noise, whose high frequency component must be removed, or at least damped, prior to the calculation of the spatial derivatives of velocity.

A two-dimensional homogeneous Gaussian filter is used to smooth instantaneous PIV velocity fields. Such a filter may not be entirely appropriate for turbulent flows with statistically inhomogeneous directions, as the character of such a filter does not change as a function of the inhomogeneous coordinate. However, the use of a homogeneous Gaussian filter was not a problem in the present study because most of the structures detected were located within a layer of the observed flow region shallow enough to assume the mean velocity field was quasi-homogeneous in this layer (see section 3.4). Note that using alternative discrete spatial filters (Trapezoidal, Simpson, Najjar and Tafti 1996) did not change the main trends in our experimental data.

However, filtering may also concomitantly alter some part of meaningful physical information. According to the nature of the information sought, the question is always to know what level of information "degradation" is acceptable. Our strategy was to restrict the attenuation of energy resulting from filtering to a user-defined percentage of the energy contained in the original data. More precisely, our program performs a two-dimensional discrete Fourier transform of every raw velocity field composing the analysed PIV sequence. The same procedure is applied to the low-pass filtered velocity data obtained from an initial value of the filtering kernel width. The results are finally displayed as a unique non-dimensional spectrum representing the average distribution of energy attenuation in wave number space. Thus, the user can better estimate which scales are most

affected by filtering and which are left intact, and then decide whether the width of the filtering kernel should be altered.

2.1.2 Computation of velocity derivatives

Velocity derivatives required in the calculation of the tensors S and Ω forming the symmetric and antisymmetric part of the velocity gradient tensor, respectively, are inferred from differentiating velocity fields using a classical second order central difference scheme. The method was compared with a fourth order accurate Hermitian scheme. Computational problems arising from noisy experimental data or from instantaneous velocity fields exhibiting abrupt flow directional changes were minimized with the second order difference scheme. This led, however, to a slight smoothing out of gradient fields. Accordingly, the dynamic range of vorticity estimated by using the second order scheme was slightly narrower than with the Hermitian scheme. No other significant differences could be observed in the statistical results obtained after complete post-processing of our data. The small discrepancies that occur when the analysed velocity fields have not been filtered vanish after filtering.

2.2 Extraction of swirling patterns (step 2)

Educing coherent structures from background turbulence does not rely on one unique and systematic method. The technique used to determine when and where certain structures are passing or are present is actually related to the definition adopted for these structures. Equally, some techniques may impose implicitly a certain observation reference frame, which constraints the range of detectable structures. Mature enough techniques call for conditional sampling, wavelets, pattern recognition, proper orthogonal decomposition, stochastic estimation, or topological approaches. For a general overview and a comparison of several coherent structure eduction methods, we recommend Bonnet et al. (1998) or Bonnet and Delville (2002).

The identification method applied in the present work, which assumes implicitly that vorticity is concentrated in cores, relies on the definition of a vortex adopted by Hussain (1986). It starts with the detection of the position of vortex core centres. This stage uses the so-called λ_2 criterion of Jeong and Hussain (1995). A translational velocity is then estimated for every detected vortex core. The convection velocity of a vortex is subtracted from the total field in which the vortex has been detected before the topological and energetic features of that vortex are analysed.

2.2.1 Location of vortex core centres

Introduced by Jeong and Hussain (1995), the λ_2 criterion has the advantage of discriminating between swirling and shearing motion (Bonnet and Delville 2002), which is not achievable by visualizing only vorticity. The λ_2 criterion relies on the basic assumption that a vortex core centre is associated with a local pressure minimum. It is derived from the equation verified by the Hessian of pressure $\partial^2 P / \partial x_i x_j$, this quantity providing information about pressure extrema. The equation is obtained by applying the gradient operator on the Navier-Stokes equations:

$$\frac{d}{dt}\left(S_{ij}\right) - \nu \frac{\partial^2 S_{ij}}{\partial x_k \partial x_k} + \Omega_{ik}\Omega_{kj} + S_{ik}S_{kj} = -\frac{1}{\rho}\frac{\partial^2 P}{\partial x_i \partial x_j} \tag{1}$$

where S_{ij} and Ω_{ij} are the components of the symmetric deformation rate tensor and the antisymmetric spin tensor Ω, respectively. Although the first and second terms of equation (1) reflect mechanisms that influence the spatial distribution of pressure, they are not linked to any vortical motion. These terms represent unsteady irrotational straining and viscous effects, respectively, that Jeong and Hussain (1995) deliberately discriminate by attributing to the sum $S_{ik}S_{kj} + \Omega_{ik}\Omega_{kj}$ the occurrence of pressure minima due solely to swirling motions. Denoting by $\lambda_1 \geq \lambda_2 \geq \lambda_3$ the three eigenvalues of this tensor, a variational analysis shows that pressure reaches a local minimum if, and only if, two of these eigenvalues are negative. The equivalent condition $\lambda_2 < 0$ was thus proposed by Jeong and Hussain (1995) for the definition of a vortex core, a local minimum of the λ_2 field being associated with the local pressure minimum that is found in the core of a vortex. Since PIV velocity fields are usually two-dimensional, an equivalent 2D form of the full tensor $S_{ik}S_{kj} + \Omega_{ik}\Omega_{kj}$ is computed in the plane in which the PIV data lie. Denoting by $\lambda_1 \geq \lambda_2$ the two eigenvalues of this 2D tensor, λ_1 and λ_2 must be such that $\lambda_1 > 0 \geq \lambda_2$ to ensure the existence of a vortex core.

The approach of Jeong and Hussain (1995) has the advantage of being frame independent, meaning that vortex identification does not require the *a priori* choice of a reference frame to visualize the detected vortex cores. Thus, the technique overcomes one of the limitations of Galilean decomposition. Adrian et al. (2000) recognized that this method was a useful means of identifying eddies and calculating reliable vortex statistics. Unfortunately, its application to two-dimensional PIV velocity fields is not completely rigorous. Recall that the approach of Jeong and Hussain (1995) implicitly relies on the assumption of a zero divergence of velocity. However, the

condition $\partial U/\partial x + \partial W/\partial z = 0$ may not be fulfilled at every point of 2D instantaneous velocity vector fields obtained by PIV. This is obviously the case in our experiments as the main flow undergoes a strong acceleration in the direction normal to the observation planes so that $\partial V/\partial y \neq 0$.

Computed λ_2 fields exhibit small-scale disturbances due to numerical noise that must be damped to remove local minima of λ_2 that could be wrongly interpreted as vortex core centres. Therefore, λ_2 fields are first smoothed out by application of a two-dimensional homogeneous Gaussian filter. However, even after filtering, the application of the λ_2 criterion on 2D vector fields still returns negative peaks of λ_2 that are not all relevant as some of them do not correspond to large values of the enstrophy field. According to Schram et al. (2004), this illustrates the fact that, when three-dimensionality develops, the λ_2 criterion can wrongly indicate the presence of a vortex. These peaks are removed by setting a threshold and by retaining only the values of λ_2 such that $\lambda_2 < \lambda_{2,\text{threshold}}$. Our program does this but it is difficult to choose an appropriate value for the threshold. Structures may be missed if a too severe threshold is applied. In the opposite case, swirling patterns with a low degree of coherence or patterns difficult to class because they exhibit two or more centres can be educed. Clearly, a weakness of the present extraction method is the dependence of the number of detected structures and, possibly, of the statistical characteristics of these structures on the value of $\lambda_{2,\text{threshold}}$.

The method used in the present study consists of removing the values of λ_2 whose absolute value is lower than a user-specified percentage $\lambda_{2,\%}$ of the absolute value $|\lambda_{2,\min}|$ of the absolute minimum of λ_2 over the current instantaneous velocity field. The same percentage is applied to every snapshot with the aim to investigate the largest possible range of vortices. From a visual inspection of several velocity fields, the method was found appropriate to remove the lower values of $|\lambda_2|$ due to either residual numerical noise or bulk flow directional changes with a large curvature radius that we could not associate with coherent eddy structures. One possible drawback of this technique is that apparently coherent patterns exhibiting a low vortical intensity are sometimes not detected if they appear on velocity fields embedding other vortices with a high energetic content whereas they would be retained in velocity fields containing eddy structures with, on average, a lower energetic content. However, as the PIV velocity vector maps in this study included velocity fields devoid of highly energetic structures, this shortcoming was statistically compensated for to some extent by the large number of snapshots recorded for analysis.

2.2.2 Galilean transformation

Another drawback of the technique described above is that we cannot rely on the λ_2-fields to analyse the topological features of all detected vortices. Concentrated regions of negative values of λ_2 are sometimes truncated by the application of a threshold. This is why the topological features of the detected vortices are estimated from an examination of the spatial distribution of velocity around the corresponding vortex core centres (see section 2.3). This imposes that each detected vortex must be analysed in a frame that moves at the same velocity as the core of the vortex. The translational velocity of a vortex is here taken as the velocity measured at its centre. It is subtracted from the total instantaneous velocity field in which the vortex appears prior to the examination of the characteristics of this vortex. Schram et al. (2004) used a reference frame moving with an average velocity calculated over the core dimension. Alternatively, one can use the local mean velocity, which is close to the velocity at which a vortex frequently moves.

Whatever convection velocity is used, all the methods above assume implicitly that a vortex core is transported at a uniform velocity, which is not exactly true. Thus, subtracting a uniform convection velocity from the velocity field in which a vortex is embedded may not always provide a fully accurate picture of the vortex. This can be illustrated by using the synthetic velocity field induced by a Taylor-Green vortex. When the vortex is transported by either a uniform flow or a pure shear flow, the apparent velocity field no longer exhibits a circular pattern although, in both cases, the λ_2 criterion indicates the existence of a vortex centre at the mesh point where the Taylor-Green vortex was placed initially. However, by viewing the detected structure in a reference frame moving uniformly at the vortex centre velocity, the initial Taylor-Green vortex is retrieved exactly only in the case of a vortex transported by a uniform flow (Figure 1a). In the other case, a distorted structure, different from the initial Taylor-Green vortex, is revealed (Figure 1b).

In practice, it is hard to estimate the error made in using a uniform convection velocity when one should not. It depends on the size of the vortex to which the procedure is applied, on the spatial characteristics of the actual transporting velocity field, and on how far this velocity field departs from a uniform velocity field. By removing a uniform convection velocity, it is not possible to say if the deformation possibly observed on the structure resulting from this Galilean transformation is also present on the initial vortex or if it results from an inappropriate choice of the transporting flow field. In the experiments described below, the mean flow velocity in the region where most vortices were detected was almost zero and could be assumed uniform locally. The error made in analysing the detected vortices in reference frames moving at a uniform convection velocity may be therefore negligible in first approximation.

2.3 Vortex characteristics (step 3)

2.3.1 Size and shape

The size of a vortex is determined by examining the distribution of tangential velocity V_θ around the vortex centre. It is assumed that a vortex core is marked by an increase in tangential velocity with radial position inside the vortex, and a decrease in tangential velocity with radial position outside the vortex.

The size and shape of a detected structure is estimated numerically by finding the maximum of V_θ along 8 radial directions defined by the angle they form with the horizontal axis (Figure 1a):

- 0° and 180° (horizontal direction, referred to as direction 1 or simply $\alpha = 0°$);
- 45° and 225° (first diagonal direction, referred to as direction 2 or simply $\alpha = 45°$);
- 90° and 270° (vertical direction, referred to as direction 3 or simply $\alpha = 90°$);
- 135° and 315° (second diagonal direction, referred to as direction 4 or simply $\alpha = 135°$).

As the method relies on an examination of the low-pass filtered velocity fields, it has the advantage of processing almost raw information that has not undergone multiple and successive transformations. It is not too selective, as the topology of the detected structures is not constrained by any pattern model. In particular, it detects anisotropic structures, ranging from closed elliptical patterns to structures open in one or more directions. One possible drawback is that the exact shape of larger vortices may not be assessed with the same accuracy as for smaller scales since the number of directions along which we search for the maximum tangential velocity is the same for all scales. This can be alleviated by increasing the number of directions and/or by implementing refining schemes to enhance the accuracy of the method at a sub-grid level (Agrawal and Prasad 2003). Though not difficult, this approach has been postponed to a later stage. Consequently, the accuracy in the determination of the mean diameter of the detected structures is here limited by the spatial resolution of our PIV snapshots, and is a multiple of it.

To account for non-isotropic closed vortices, four diameters D_α (α=0°, 45°, 90°, 135°) are estimated for each detected vortex from the sum of $R_{\alpha 1}$ and $R_{\alpha 2}$, the vortex radii defined as the distance to the vortex centre from the point where, in the considered direction α, V_θ reaches a maximum. From this, it is inferred for each vortex:

- a mean diameter: $D_m = \frac{1}{4} \sum_{\alpha=0,45,90,135} D_\alpha$ (2)

- an eccentricity: $\chi = \frac{\max(D_\alpha)}{\min(D_\alpha)} \qquad \alpha = 0°, 45°, 90°, 135°$ (3)

2.3.2 Nature of structures

As stated in section 2.2.2, artificial topological distortions might arise from the use of a uniform convection velocity in the Galilean transformation applied in our analysis sequence. Vortices undergoing deformation by stretching, compression, or shear, or structures with their axis misaligned with the normal to the measurement plane also tend to give swirling patterns with radial profiles of tangential velocity deviating from the ideal case. This is also true of coherent structures captured as they are losing their spatial integrity. Therefore, our algorithm distinguishes between the following cases:

- Case 1: the tangential velocity distribution of a swirling pattern is no longer axisymmetrical but still presents a maximum whatever radial direction is considered. The radii $R_{\alpha 1}$ and $R_{\alpha 2}$ may vary with α, but the considered structure remains perfectly closed. Such a structure is referred to as a *closed vortex* or, more simply, a *vortex*.
- Case 2: a maximum of V_θ cannot be determined in one or more radial directions. Corresponding open structures are referred to as *vortices of first, second, third or fourth type* according to the number of open directions. The mean diameter of second, third and fourth type vortices is estimated without taking into account open directions. Nor are these directions taken into account in the estimation of eccentricity. In the statistical analysis, open structures are considered separately.

In our method, a swirling pattern is labelled “closed” after consideration of only a fraction of the total number of grid points that this pattern comprises, excluding those points that do not lie along the above 8 radial directions but still fall within the boundary of the vortex. This leads to a certain inaccuracy about whether a detected structure is really closed, especially at large radii. Thus, our approach may not appear as elegant and accurate as, for example, that of Agrawal and Prasad (2002a, 2002b, 2003). However, it has the advantage of being less selective by allowing the characterization of a broader variety of patterns, including non-symmetrical ones, which is precluded by the method of Agrawal and Prasad (2002a, 2002b, 2003).

2.3.3 Energy content

The vortical intensity I_v (or area-averaged vorticity, or average vorticity) of a vortex core of surface area S_v is defined by $I_v = \Gamma / S_v$. The quantity Γ (equation 4) is the vorticity flux across S_v. The square of Γ is proportional to the energy of the considered vortex.

$$\Gamma = \int_{S_v} \vec{\Omega} \cdot \vec{n} dS \tag{4}$$

where $\vec{n}$ is the unit vector normal to the surface S_v, and $\vec{\Omega}$ denotes the vorticity vector that here reduces to $\Omega\vec{n}$ with Ω the out-of-plane component of $\vec{\Omega}$. By applying Stokes theorem to the gridded PIV velocity data, Γ is estimated from:

$$\Gamma = \oint_{L} \vec{U} \cdot d\vec{l} \tag{5}$$

where L describes a closed path of integration around the surface S_v. Equation (5) is evaluated using the trapezoidal approximation. The path of integration is an ellipse centred at the vortex core centre and formed from both the minimum and maximum of D_α. A bi-linear interpolation of the velocity on this contour is performed. The vortical intensity I_v of a vortex core is finally obtained by dividing Γ by the surface area of the ellipse.

The vortical intensity I_v of a vortex is homogeneous to a frequency (s^{-1}). It can be associated with the revolution time t_r of a vortex around its own axis. This characteristic time scale can be compared to the time scale t_d representative of diffusive mechanisms occurring at the scale of the vortex core. This time scale t_d can be estimated by $t_d \equiv R_v^2 / \nu_e$ where R_v denotes the mean vortex radius, and ν_e is the effective viscosity. The degree of coherence of a vortex, from a schematic point of view, can be assessed from the ratio of these two characteristic time scales. When $t_d / t_r >> 1$, a structure can be considered coherent as diffusive mechanisms do not affect significantly the thickness of a vortex core over several vortex revolutions (Chassaing 2000).

2.3.4 Other sources of error and effects of resolution

The accuracy of our PIV technique is determined primarily by the error in locating the correlation peak to subpixel accuracy. Our estimated value is about $1/64^{th}$ of a pixel. In a typical run, the maximum velocity, U_{max}, encountered in the measurement planes lies between 1 and 4 m/s. This

corresponds to a particle displacement of 4 pixels. Therefore, the error in the instantaneous velocity measurement is about 0.004 U_{max}. Details regarding the identification and replacement of spurious vectors that can affect the measurements discussed here are given in section 3.4. Overall, only 3% of the vectors were rejected and substituted. Thus, we do not expect a substantial influence of the replaced vectors on our results.

Errors can arise from other sources. For example, it is probable that a true vortex centre will not fall exactly on a grid point. The worst case occurs when the actual centre falls between adjacent grid points. The maximum error is therefore equal to half of the grid spacing (about 0.5 mm here). Consequently, due to the discretizing nature of the eduction process, the vortex radii may be slightly smaller or larger than the estimated values. As we are averaging over hundreds of vortices, it is likely that these discrepancies will cancel to some extent. Nevertheless, the results presented in this paper must be interpreted bearing in mind these specificities of our eduction method.

Our PIV measurements are necessarily limited to the range of spatial scales that can be resolved due to the finite size of the measurement window and of the interrogation areas. In the present measurements, for example, with Re = 14000 and H/e = 10, the Kolmogorov scale, η, for the flow is of the order of 0.05 mm whereas we can only resolve structures larger than about 1 mm. The Kolmogorov scale was derived from the correlation established by Antonia et al. (1980) in the self-preserved region of a plane free jet. This correlation, of course, does not hold in the present case. It nevertheless provides a very rough idea of the order of magnitude of the upper limit of η.

Agrawal and Prasad (2002a) showed that the smaller unresolved scales do not affect the vortex population statistics computed for the larger resolved scales even though the lack represents a gap in the data at the smaller scales, characterized by a somewhat premature drop-off in the pdfs as one approaches small values of the computed quantities. This issue was not examined in greater detail as, in the present study, smaller scales represent only a small proportion of the coherent structures exposed by our algorithm.

3 Test case

3.1 Experimental set-up

The experimental facility used in this study consists of a 6 m long horizontal open tunnel with a 0.3 m x 1 m cross-sectional area. Only half of the set-up is depicted in Figure 2, the installation

being symmetric geometrically. The front wall and the floor of the tunnel are transparent to allow PIV measurements. The floor-to-ceiling clearance can be varied to cover different values of the opening ratio H/e where H is the nozzle-to-plate distance and e is the nozzle width.

Each blowing unit consists of two fully independent feeding circuits. It can be operated in single jet or twin-jet air mode. The so-called exterior jet is always fed with air from the laboratory. The interior feeding circuit can be operated in a closed-loop mode to form a fully or partially recirculated air curtain. In this case, the interior jet is fed with air from inside the tunnel. The terminal diffuser has a 10:1 contraction ratio. The splitting plate in the diffuser is 0.5 mm thick. The exit section of the blowing unit is 0.03 m wide. The discharged air streams are always blown vertically downwards, spanning the wind tunnel cross-section completely.

When the blowing unit is operated in the twin-jet mode, the initial velocity of each jet can be adjusted independently in the range 1 m/s to 15 m/s by varying the rotation speed of the fans. A monitoring system consisting of 1.5 mm outer diameter total head tubes connected to standard micromanometers provides on-line information about outlet velocities. The signals from the pressure transducers are systematically recorded during measurements. The turbulence level at the nozzle exit is about 1 %. Qualification and validation experiments showed that the flow at the nozzle exit was highly uniform in the spanwise direction (Gupta 2005).

3.2 Test configuration

Numerous experiments involving various air curtain arrangements have been performed (Gupta 2005). Here, we shall consider only one test-configuration for the purpose of illustration. In this case, the system was operated in the twin-jet mode. Both supply circuits were fed with air taken from the laboratory room. The outlet velocity U_0 at the nozzle exit was 7 m/s for both jets. Thus, the Reynolds number based on e and U_0 was 14000. Both tunnel outlets were open to the ambience.

The above flow configuration is very similar to a single jet with an opening ratio H/e of 10. The main difference lies in the presence of Kármán instabilities in the initial region of the main flow, at the interface between the two individual jets forming the air curtain. These wake structures, which develop downstream of the nozzle splitting plate, vanish at a distance of about $5e$ (Gupta 2005).

3.3 Overall view of the main flow in the xy-plane

Figures 3a to 3f provide a general picture of the main flow structure in the xy-plane. Details about the relevant PIV measurements can be found in Gupta (2005). The dashed lines in the figures show the position of the xz-planes in which 2D-traces of eddy structures were subsequently sought. From Figures 3a and 3b, it can be seen that the jet deviates slightly to the right. The stagnation line is located at $y/e \approx 0.4$. From a careful examination of the jet sensitivity to various imposed far-field boundary conditions, the jet deflection could be attributed to the fact that the air curtain was not located at an equal distance from the two far ends of the tunnel (Gupta 2005).

The two canonical jets forming the air curtain are clearly distinguishable in Figure 3a. A closer look at the nozzle exit velocity profiles would reveal almost top-hat profiles for each jet. The length of the potential core of each jet is close to $5e/2$, which is equal to what would be observed in the absence of the other jet. From $x/e \approx 5$ up to around $x/e \approx 8$, the spatial distribution of mean velocity compares fairly well with the distribution obtained for a single impinging jet with an opening ratio of 10. It looks as if the flow has lost memory of the upstream flow structure.

By comparison with a single jet, the presence of a wake increases turbulence activity in the initial flow region between the two issuing jets. However, the jet centre plane exhibits average turbulence levels much lower than within the two lateral shear layers where, apart from the impact region, most of the turbulent activity remains concentrated (Figures 3c-f).

Within the impingement region, there is a relatively "calm" zone of average diameter about e. Maxima of turbulent kinetic energy are concentrated in a band that coincides with a stronger curvature of streamlines. In this region, the contribution of the fluctuations of the longitudinal and transverse components of velocity to turbulent kinetic energy is comparable.

3.4 PIV measurements in xz-planes

Our eduction algorithm was applied to instantaneous velocity fields measured in about 6 cm × 6 cm vertical xz-planes within the impingement region at 5 locations with respect to the distance from the jet central plane (Figure 4). The dimensions of the observation window were chosen in accordance with the jet nozzle dimensions and with the expected size of the coherent structures possibly present in this flow region. They were large enough to ensure that, potentially, a sufficient number of eddy structures could be observed in every snapshot. The height of the observation windows is greater than the depth of the impingement region, which does not extend further than about 13% of the nozzle-to-plate spacing in the jet central plane (Maurel et al. 2004).

The flow was illuminated from below by a Quantel BrilliantB double cavity pulsed Nd:YAG laser operated at 532 nm. Each laser shot delivered up to 120 mJ with a pulse duration of 10 ns. The beam from the laser was passed through a series of spherical and cylindrical lenses to achieve a light sheet less than 1 mm thick. Digital images were recorded with a Kodak Megaplus ES 1.0 cross-correlation camera with a digital resolution of 1008 x 1016 pixels^2 that viewed the light sheet from a distance of about 15 cm.

The seeding consisted of an aqueous glycerol solution. It was delivered into the jet by injecting the particles upstream of the blowers, and into the entrained air by using multi-hole pipes suitably positioned in the far field on either side of the air curtain. Conditional sampling, i.e. velocity bias arising from entrained air containing no particles, was thus obviated. Particle sizing of the smoke showed that 95 % of the particles had diameters below 5 μm, which was more than adequate in this case.

Pairs of images were recorded at a rate of 15 Hz. The interrogation areas were cross-correlated. A Gaussian window function was applied to the interrogation areas to minimize phantom correlations near their edge. A subpixel interpolation scheme was used to resolve particle displacement to 1/64 of the pixel pitch on the CCD array. Peak-height, velocity range and moving-average validation procedures were applied successively after cross-correlation of the images. Table 1 presents the recording parameters of the PIV system used in our experiments.

3.5 Mean flow characteristics in xz-planes

Figures 5a-e represent contour plots of mean normalised velocity magnitude in the 5 vertical planes of interest in this paper. The flow is rather homogeneous in the z-direction for y/e = 0 (nozzle symmetry plane) and y/e = 1. The mean flow velocity decreases almost linearly with decreasing distance from the impingement plate. A departure from these two homogeneous situations appears at y/e = -1, i.e. on the jet side opposite to the direction of the jet deflection. The departure is more pronounced at y/e = ±3 (Figures 5a and 5e). The reasons for which the flow homogeneity in the spanwise direction deteriorates as the distance from the impact region increases are still not fully understood. This would require a more careful inspection of the flow in these regions. In Figures 5a and 5e, the decrease in velocity magnitude with increasing distance from the wall indicates that relevant measurement planes correspond to cross-sections in the developing region of the wall jets that form on both sides of the main jet after impingement.

Figure 5f, which is rather representative of what can be observed in the four other measurement planes, shows the scalar field of $\partial\overline{U}/\partial x + \partial\overline{W}/\partial z = -\partial\overline{V}/\partial y$ normalised by e/U_0 at $y/e = 0$. Negative values reflect that, because of the jet deflection, the measurement plane at $y/e = 0$ does not coincide exactly with the air-curtain central plane. In the present case, negative values indicate that the flow is accelerated towards the front end of the tunnel. The out-of-plane elongational strain decreases with increasing distance from the impingement plate. The higher values lie in the region where most vortices have been detected. Figure 5f shows to what extent the considered mean velocity fields and, especially, the analysed instantaneous velocity fields are far from being divergence free.

4 Vortex eduction

4.1 Discussion about user-specified parameters

Parametrical tests were carried out to investigate the individual influence of the 3 user-specified parameters in our algorithm. These tests were performed directly on the velocity vector fields recorded in our experiments instead of too idealized analytical velocity fields in which it would be difficult to fully embed the whole complexity of the flow considered here. Very similar observations were made for all the measurement planes. Therefore, only the results obtained for $y/e = 0$ are reported and briefly discussed below.

4.1.1 Velocity-field filter size (step 1)

The width of the filtering kernel applied to the instantaneous velocity fields was varied between 3 × 3 and 13 × 13 grid points with a constant standard deviation of 0.65 times the filter box size. The width of the filtering kernel applied to the λ_2 fields and the threshold $\lambda_{2,\%}$ were set to 7 × 7 grid points and 20 %, respectively, to "visualize" the effects of varying the width of the filtering kernel applied to the velocity vector fields over as large a range of scales as possible.

Figure 6 gives a picture of the ratio $P(k)/P_0(k)$ obtained after application of a Gaussian filter of size 7 × 7 grid points where $P(k)$ and $P_0(k)$ denote the ensemble-averaged power spectral densities of turbulent kinetic energy computed at wave number k (m^{-1}) with and without filtering, respectively. Figure 6 shows that a filter of size 7 × 7 grid points leads to an energy attenuation greater than 30 % only at wavelengths shorter than or equal to about 3 mm ($\log(k) = 2.5$). This was acceptable in the present case in view of both the expected size of the coherent structures sought and the smallest

resolvable scales. The average attenuation of the total turbulent kinetic energy contained in our raw velocity vector maps was about 18 % (see Table 2). For comparison, Geers et al. (2005) retained only the first 20 modes of the proper orthogonal decomposition used to construct the inhomogeneous low-pass filter they applied to their PIV velocity fields. By doing so, about two thirds of the total energy of velocity fluctuations was removed from their original snapshots.

The results reported in Table 3 show that smoothing has a marked influence on the total number of structures detected over our test sequence of velocity vector fields. As expected, this number decreases as the size of the filter applied to the analysed vector maps increases. Simultaneously, the proportion of closed structures increases whereas that of structures with one or more open direction decreases due to the removal of local discontinuities in the velocity fields. The unrealistically high number of coherent structures exposed on average over an instantaneous velocity field at the lower filtering kernel widths is due to the low values assigned to the two other user-specified parameters.

The histograms of D_m show that the application of a filter of increasing size results in a consistent diminution of the contribution of all detected scales and not only of the lower scales. The upper bound of the histograms of D_m shifts towards the higher values of D_m as the width of the filtering kernel increases. This leads to the increase in the median and the mean of the pdf of D_m reported in Table 3. The histograms of χ reveal that larger filter kernels result in narrower distributions, i.e. in a lesser dispersion in terms of structure shape. Simultaneously, both the median and the mean of the pdf of χ decrease slightly with increasing filter width (Table 3).

The histograms of I_v show that the range of vortical intensity in the analysed sequence decreases noticeably when the size of the filtering kernel is increased. In fact, the higher values of vortical intensity are set by the lower scales that are related to local non-uniformities in the analysed velocity fields, and that filtering removes efficiently. It was checked that filtering does not affect significantly the range of vortical intensity associated with the structures sought.

4.1.2 λ_2-field filter size (step 2)

Gaussian filters of increasing size were applied on the fields of λ_2 (from 3 × 3 to 13 × 13 grid points with a constant standard deviation of 0.65 times the filter box width). In this test, the width of the filtering kernel applied to the velocity fields was set to 7 × 7 grid points with a standard deviation of 0.65. The threshold value $\lambda_{2,\%}$ was kept constant at 20 %.

Filtering results primarily in a decrease in the total number of detected vortex core centres (Table 4). However, it leaves almost unchanged the position of the main peaks of negative λ_2 as long as not too severe a filter is used. Applying too large a filtering kernel may result in the progressive replacement of initially separated peaks by a single peak, which also contributes to the decrease in the total number of detected vortex centres. Thus, algorithms based on the examination of fields of λ_2 to characterize the size and shape of swirling patterns should make use of filtering carefully. This is why, in the present case, the λ_2 criterion was used only to detect vortex core centres and not to characterize the topology of the detected structures.

By removing the lower scales associated with spurious local minima of λ_2 (noise) and simultaneously eliminating the larger scales corresponding to the low iso-λ_2 islands present before filtering, filtering has eventually no influence on the median values of D_m and χ. Nor is filtering selective with respect to the vortical intensity of the detected structures, as shown by the pdf of I_v.

4.1.3 Threshold value, $\lambda_{2,\%}$ (step 2)

Theoretically, the parameter $\lambda_{2,\%}$ allows the user to eliminate the less significant peaks of λ_2, which are not all relevant as some of them do not correspond to large values of the enstrophy field. The question, however, is what does "large values of the enstrophy field " mean? There is no absolute reference. Therefore, in practice, for a given flow configuration, the decision about where to set the limit between a relevant and an irrelevant peak of λ_2 (i.e. low or large values of the enstrophy field) is left to the user. This choice may be significant.

In this test, the width of the filtering kernels applied to both the velocity fields and the λ_2 fields were set to 7 × 7 grid points. The value of $\lambda_{2,\%}$ was varied between 10 % and 60 %. Table 5 shows that increasing the value of $\lambda_{2,\%}$ results in a sharp decrease in the total number of detected vortex core centres. The histograms of D_m show that the number of larger scales decreases more rapidly than the number of lower scales as $\lambda_{2,\%}$ is increased. This is because the lower peaks of λ_2 are mainly located at the centre of relatively large iso-λ_2 islands in which, on average, λ_2 has moderate values. Consequently, the median of the pdf of D_m decreases as the proportion of lower scales increases with $\lambda_{2,\%}$ (Table 5). However, the rms value associated with the variations of the median of D_m with $\lambda_{2,\%}$ is about only 5 % of the mean value of the median of D_m over the present test.

By increasing the value of $\lambda_{2,\%}$, the proportion of closed patterns increases while the proportion of structures with only one open direction decreases. The sum increases slightly. Thus, the structures that exhibit the lowest spatial coherence are efficiently removed. Simultaneously, the median of the pdf of χ decreases slightly (Table 5). Interestingly, the process seems to have a stronger influence on the number of structures detected far from the impingement plate. This implies that the vortical patterns located in this flow region may not correspond to coherent structures. They are efficiently discriminated. However, by eliminating these patterns, perhaps we are missing information here about forming and evolving regions of concentrated vorticity or swirling patterns.

In Schram et al. (2004), a single value of the threshold $\lambda_{2,\text{threshold}}$ bearing on all the λ_2-fields computed over a sequence of velocity vector maps was used and applied indistinctively to every λ_2-field. This value was chosen on the basis of the pdf of the negative values of λ_2 computed over the entire set of analysed vector fields. It was found that a value of $\lambda_{2,\text{threshold}}$ equal to twice the standard deviation of the pdf of λ_2 gave a good compromise concerning the number of detections and the robustness. Note that the criteria for a good compromise and for robustness were not specified. In the present case, through the use of a unique value of $\lambda_{2,\%}$, distinct values of $\lambda_{2,\text{threshold}}$ were implicitly determined for each velocity vector map so as to take into account the variations of $\lambda_{2,\text{min}}$ over a given sequence of velocity vector maps. The pdf of the values of $\lambda_{2,\text{threshold}}$ obtained from the data set used in the present test was computed. We found that the mean value $\overline{\lambda}_{2,\text{threshold}}$ and the standard deviation of the pdf of $\lambda_{2,\text{threshold}}$ converge statistically when the number of analysed velocity vector maps was greater than or equal to 100. The value of $\overline{\lambda}_{2,\text{threshold}}$ obtained in the present case was compared to that obtained by using the method of Schram et al. (2004). It was found that $\overline{\lambda}_{2,\text{threshold}}$ was closer to 2.5σ than to 2σ, where σ is the standard deviation of the pdf of Schram et al. (2004). This is illustrated in Figure 7 where the results of this analysis in the 5 measurement planes are all reported. Thus, although it is slightly more severe, our approach is rather consistent with that of Schram et al. (2004), justifying our choice.

4.2 Application

Finally, Gaussian filters of size 7 × 7 grid points with a standard deviation of 0.65 times the filter box size were used for both the velocity and λ_2 fields. A threshold of 40 % of the absolute minimum of λ_2 encountered on each velocity vector map was used. With these values, the mean diameter and the vortical intensity of detected structures were estimated with an average relative uncertainty of about ± 10 %, although this is difficult to quantify accurately. With these settings, it was possible to

retain efficiently most of the coherent patterns present in the flow under investigation while preserving their main features. Note finally that less than 1% of the total number of patterns exposed in the low-pass filtered fields was detected in the high-pass filtered fields obtained by subtracting the low-pass filtered fields to the instantaneous fields. This is not too surprising considering both the size of the viewframe ($\approx 60 \times 60$ mm^2) compared to the width of the jet nozzle (30 mm) and the cut-off filter size applied to the velocity fields.

The results presented below concern closed vortices only. However, most of the tendencies described would not be affected significantly by including open type vortices in the analysis. The jet nozzle width, e, and the jet exit mean velocity, U_0, are used to normalise the plotted quantities.

4.2.1 Vortex size and shape

The total number of vortices detected in each measurement plane was typically of the order of 2000. A different number of vortices was captured in each frame, implying that the distribution of eddies over time is somewhat random. No noticeable trend for the number of vortices in successive frames was apparent, confirming that the flow conditions were indeed stationary.

On average, about 4 to 5 coherent structures were exposed per instantaneous realization. This is much lower than the 49 eddies per frame found on average by Agrawal and Prasad (2002a and 2002b) in the axial plane of a self-similar turbulent axisymmetric jet (46 vortices in the high-pass filtered fields and 3 in the low-pass filtered fields). However, any comparison between our results and those of Agrawal and Prasad (2002a and 2002b) should be considered with caution. The observation scale is different, as the ratio of the size of the viewframe to the jet nozzle width is 2 and 65 in the former and the latter case, respectively. Moreover, in the present case, the focus was on the coherent part of the vortices present in the flow region under investigation. We are therefore resolving a portion of the entire length-scale spectrum narrower than Agrawal and Prasad (2002a and 2002b) who were more interested in revealing the largest possible spectrum of structures present in their flow. The authors have independently discussed the large and small vortices by separately inspecting the low-pass and high-pass fields, respectively.

About 70 % of the detected structures are closed vortices while 25 % correspond to first type open structures (Figure 8a). The proportion of open structures tends to increase slightly with distance from the plane at $y/e = 0$ as though the structures present in the jet central plane tend to lose their integrity as they are carried away from this plane by the lateral wall jets that develop on either side

of the impingement region. This seems to be in good agreement with the strong three-dimensional nature of the flow in this region. However, an exact description of the effects of the deformation mechanisms involved in this perturbed flow region, where the lateral mixing layers of the main jet break up and where wall jets start to grow, would require a more thorough local analysis.

The smoothed pdf of D_m/e are plotted in Figure 9 for the 5 values of y/e considered here. On average, the standard deviation of the pdf of D_m is about 3.4 mm. Figure 9 shows that a broad range of structures coexist in the impingement region, most of them with a mean diameter of between 4 and 14 mm, i.e. between about $e/10$ and $e/2$. Our results tend to confirm the numerical observations of Beaubert (2002) and Yokobori et al. (1977) who noticed the presence of isolated secondary vortex tubes of smaller diameter between much larger vortex pairs. Considering the uncertainty in the determination of D_m, it would be premature to conclude about preferential vortex sizes in each measurement plane from the bumps visible in Figure 9.

The mean $\overline{D_m}$ of the pdf of D_m, ranges between $0.25e$ and about $0.3e$. It is minimum at $y/e = 1$ (Figure 8b). This minimum occurs approximately at the position of the jet stagnation line, recalling that in the present experiments the jet was slightly deflected to the right, i.e. towards the positive values of y/e. $\overline{D_m}$ increases almost linearly with distance from the plane $y/e = 1$, indicating that the probability of finding larger structures increases with distance from the position of the jet stagnation line. Finally, note that the mean of the pdf of D_α ($\alpha = 0°, 45°, 90°, 135°$) follows the same trend as $\overline{D_m}$ (Figure 8c).

If we assume that the 2D patterns visualized in our planes are traces of roll cells with their axis perpendicular to the jet, the observed increase in $\overline{D_m}$ with distance from the plane at $y/e = 1$ may reflect a tendency for these structures to grow in size as they stretch in the lateral wall jets. The fact that the total number of detected structures is almost constant with y/e, and the apparent slight decrease in the proportion of smaller structures as y/e increases (Figure 9), could also be good arguments in favour of this idea. The 3D instantaneous iso-Q and iso-vorticity contour plots stemming from Beaubert's (2002) numerical simulations of a single jet with an opening ratio $H/e = 10$ support this idea. Alternatively, the observed increase in $\overline{D_m}$ with y/e might be attributed to structural distortions leading to vortex tubes with their main axis no longer aligned with the normal to the measurement planes. Beaubert's (2002) computational results support also this second possibility. Unfortunately, Beaubert's (2002) findings cannot help discriminate between the two hypotheses above about the increase in $\overline{D_m}$ with distance from the jet symmetry plane because only

instantaneous pictures were presented in the author's report. Moreover, the corresponding numerical simulations were not performed over a sufficient time to allow reliable statistics. Further experiments involving synchronous measurements in the 5 planes investigated here or measurements in horizontal planes could bring valuable additional information in this respect.

The pdf of eccentricity, χ, does not vary significantly with *y/e*. Most of the detected vortices are characterized by an eccentricity ranging from 1 to 3. A quarter of them exhibit an eccentricity close to 1.7. The median of the pdf of χ is about 1.8 while $\overline{\chi}$ is closer to 2.05. The latter is almost constant, increasing only slightly with distance from the plane *y/e* = 1 where it reaches a minimum (Figure 8d). The main result here is that most of the vortical patterns detected in the impingement region of our jet are elliptical rather than circular. Figure 10, provided for *y/e* = 0 although similar tendencies were observed in the other measurement planes, indicates that preferential directions of deformation seem to exist. A closer inspection of the directions of the minimum and maximum diameter of the detected structures reveals that the rather large values taken by χ in all the measurement planes are primarily due to the simultaneous presence of either structures with their maximum diameter oriented at 45° and their minimum diameter oriented at 0° and 90° or vortices with their maximum diameter oriented at 135° and their minimum diameter oriented at 0° and 90°. The directions of maximum and minimum diameters are not necessarily positioned at right angles. This is partly due to the error made in assuming, in our eduction scheme, that any detected vortical structure is transported at a uniform velocity, equal to the velocity at the corresponding vortex core centre (see subsection 2.2.2). Deformations with similar orientations of the directions of minimum and maximum diameters were observed in the almost elliptical structure obtained after application of our eduction scheme to a Taylor-Green vortex embedded in a uniformly accelerated flow. However, as the structures detected in the impingement region of our jet are not immersed in a uniformly decelerated flow, the effects of true deformations add to the above artificial deformations. Nevertheless, our observations exhibit a certain consistency with the results of Maurel and Solliec (2001): their pictures of vortex pairs clearly depict elliptical structures with an eccentricity close to 2, a minimum diameter in the horizontal direction, and a maximum diameter in the vertical direction.

4.2.2 Direction of vortex rotation

Overall, the probability of finding a vortex with an anticlockwise rotation is close to that of finding a vortex with a clockwise rotation, even though a certain discrepancy in populations is visible for *y/e* = -1, 1 and 3 (Figure 8e). We checked that the observed differential is not due to sampling

errors. Curiously, the proportions of clockwise and anticlockwise rotating structures match better for all *y/e* when open structures are accounted for in the two populations. This would indicate a more pronounced tendency for the clockwise rotating structures to lose their spatial integrity, which is surprising. No correlation was found between the consistent excess of anticlockwise rotating closed structures for all planes and the observed variations of the mean flow topology with *y/e* (see Figure 5). A closer examination of the rate-of-strain tensor field would probably provide useful information. Although the systematic bias noticed in the distribution of clockwise and anticlockwise vortices has to be clarified in future experiments, it has no effect on the rest of the present analysis.

At first sight, our results could corroborate earlier observations (Maurel and Solliec 2001, Sakakibara et al. 1997) suggesting the systematic presence of counter-rotating pairs or vortices in the impingement region of a plane turbulent jet. Thus, a procedure was added to our program to check for counter-rotating structures in the immediate vicinity of any detected vortex. It was found that the eddy structures detected by our algorithm were not systematically organized in pairs of counter-rotating vortices. On the contrary, the latter were apparently not the most frequent pattern, especially in the planes at $y/e = \pm 3$. This was confirmed by a visual inspection of several individual velocity vector maps. It can be explained by the following:

- The lifetime of the structures observed in the impingement region of our jet is generally much shorter than the time separating two consecutive snapshots (see subsection 4.2.4). Therefore, the probability of detecting simultaneously the two eddy structures constituting a pair of counter-rotating vortices may not be 1.
- The PIV measurement window used in the present experiments does not span entirely the width of our tunnel. We therefore cannot exclude the possibility of vortex pairs located at the edges of the measurement window where only one vortex would be visible.

Consequently, we shall not draw any premature conclusions that would unfairly question the results of Maurel and Solliec (2001) and of Sakakibara et al. (1997).

4.2.3 Spatial distribution

A representative example of the two-dimensional probability density function of the presence of detected eddy structures is shown in Figure 11a for $y/e=0$. The distribution was simply obtained by counting the number of vortex centres detected in grid cells of about 3 mm × 3 mm (6 grid units) and by dividing this number by the total number of structures detected in the observation window.

Structures exist across the entire impingement region. However, the probability distribution of vortex occurrence is higher close to the wall. This would suggest that the coherent structures present in the wall region of the present turbulent impinging jet do not come from the upstream flow, i.e. from the jet itself or from the jet lateral mixing layers as suggested by Sakakibara et al. (1997) or Beaubert and Viazzo (2003), but rather arise in the impingement region. However, this statement should be considered with caution, as we cannot totally exclude the presence of structures in the process of formation in the upper part of our measurement window. If these evolving structures do not exhibit a sufficient degree of coherence and/or if their vorticity is too low, they can be missed by our algorithm.

Detected vortices are quite evenly distributed horizontally. The absence of regularly spaced regions exhibiting peaks of density of presence tends to preclude the possibility both of particular channels through which vortices would travel and of stationary swirling patterns. There is no indication that vortices form or stay at preferential locations. This is consistent with the apparent lateral sweeping motion of the tubular vortices present in this region reported by Beaubert (2002). Structures of all size contribute to the higher probability of occurrence of a vortex in the vicinity of the wall.

From the cumulative probability density functions of presence plotted against the distance from the wall (Figure 11b), it appears that more than 80 % of the detected structures are located within the lower half of the observation window, that is to say within a layer equal to about e or 10 % of H in the present case. This is slightly less than the depth of the flow region disturbed by the presence of the impingement wall, which was found to be around 13 % of H by Maurel et al. (2004).

Figure 11b shows that 50 % of the detected vortices are located within a relatively shallow layer of the impingement region. For y/e = 0 and y/e = 1, this layer extends up to about 9 mm above the wall. Its depth d_i is thus approximately equal to $e/3$, which here represents about 3 % of the nozzle-to-plate spacing H. In these planes, the layer in which 50 % of the detected vortices lie coincides rather well with the wall region defined by Maurel et al. (2004) as a transition region between the confinement zone where, with respect to a free jet, the main flow entrainment and expansion rates decrease and increase, respectively, and the region where the flow separates into two opposite wall jets. The value of d_i increases with distance from the nozzle symmetry plane. This is rather consistent with the observed increase in size of the detected structures with this distance. Incidentally, the value of d_i at a given y/e is of the same order of magnitude as the corresponding value of $\overline{D_m}$.

4.2.4 Circulation, vortical intensity and time scales

Figure 12a shows the value of normalised circulation, Γ, versus D_m for all detected structures in the plane $y/e = 0$. The distribution for negative eddies (anticlockwise rotating structures) is almost a mirror-image of the distribution of the positive eddies, which implies that the total number of eddies from all the individual realizations is large enough for good statistical comparisons. However, a closer inspection at Figure 12a would easily reveal a lower number of positive eddies consistently with Figure 8e. The smaller eddies exhibit a narrow range of $|\Gamma|$ while the larger eddies have a much larger range. On average, the latter have a higher value of circulation associated with them.

Figure 12b depicts the normalised pdf of Γ for all detected positive vortices as a function of the position of measurement planes. Most eddies lie below a circulation of about 0.07 m^2/s although the entire range extends to 0.15 m^2/s. The distributions of Γ obtained at a given distance on either side of the jet centre plane fall almost on the same curve, indicating a symmetrical distribution of energy. As distance from the jet centre plane increases, the histogram of Γ becomes narrower while the maximum of Γ increases, i.e. stronger vortices occur more frequently away from the heart of the impingement region. This suggests that each eddy becomes more energetic as it is transported by the wall jets developing on either side of the main jet. This result is consistent with the overall increase in $\overline{D_m}$ with distance from the jet centre plane.

The normalised pdfs of vortical intensity, I_v, are given in Figure 13a. All distributions are roughly symmetrical with a range that narrows with increasing distance from the nozzle symmetry plane. The departure from full symmetry is consistent with the excess of anticlockwise vortices for all y/e (Figure 8e). For $y/e = 0$ and $y/e = \pm 1$, i.e. for the cut planes that intersect the jet impingement region, the distributions exhibit a bimodal shape that is probably related to the presence of vortex pairs. This is no longer the case for $y/e = \pm 3$, i.e. for the cut planes intersecting the wall jet flow regions.

The normalised mean $\overline{I_v}$ of I_v is plotted versus y/e in Figure 8f. A maximum is reached between $y/e = 0$ and $y/e = 1$, i.e. in the region where the impingement stagnation line lies, and where streamlines exhibit a stronger curvature Thus, it seems to be here that the detected structures gain much of their initial rotational energy. There is then a decrease in $\overline{|I_v|}$ with increasing distance from the nozzle symmetry plane. This is rather consistent with the increase in $\overline{D}_m$ we observed, as long as it can be assumed that our structures are tubular and behave almost like solid bodies in rotation, and that angular momentum is conserved or only slightly affected during movement. Figure 13b ($y/e = 0$)

supports the idea of a larger vortical intensity at the lower scales. In a given plane, on average $|I_v| \approx \alpha D_m + \beta$. In the plane $y/e = 0$ (Figure 13b), α is roughly equal to -10^5 $(ms)^{-1}$.

The values of I_v give an idea of the revolution time t_r of the detected structures around their own axis. In the present case, t_r is from 1 to 2 ms. Thus, there is a factor of around 50 between t_r and the time that separates two successive pairs of PIV images (≈ 67 ms). From this, it is now clearer why the present approach does not allow vortex coherence in time to be assessed.

Finally, taking a mean value of 8 mm for D_m and assuming a turbulent kinematic viscosity of the order of 100 times the molecular kinematic viscosity of air, the ratio t_d/t_r defined in section 2.3.3 is about 30. Thus, from Chassaing (2000), it is fair to conclude that a certain degree of spatial coherence can be attached to the structures detected here.

5. Conclusion and perspectives

This paper is about an algorithm that was written to automatically detect and statistically characterize traces of spatially coherent eddy structures in 2D PIV velocity vector maps. This algorithm is primarily based on the λ_2 criterion of Jeong and Hussain (1995). However, this criterion is here used only to locate vortex core centres, while the topological features of a structure are inferred from an examination of the local velocity field in a reference frame moving at the velocity of the centre of this structure.

The general approach used throughout this work has the advantage that it is not constrained by any vortex model. It therefore allows the detection and characterization of structures with one or more open directions and with various shapes, which is usually not possible with other algorithms. Finally, our algorithm is independent of the observation scale. Although our method is marred by a certain number of inaccuracies, these and the errors they entail are the result of inevitable compromises. The possible adverse effects of inappropriate choices for 3 user-specified parameters present in algorithm have been highlighted.

The algorithm described in this paper was used to inspect the so far little explored wall region of a plane turbulent impinging jet with an opening ratio H/e equal to 10 at a Reynolds number equal to 14000. The analysis was carried out on velocity vector map sequences measured in 5 planes parallel to the main jet plane. Considering the accuracy of our analysis, perhaps more importance should be attached to the general trends that emerge from the results rather than to the quantitative estimates.

Strongly energetic structures covering a wide range of sizes occur together in this region, the larger eddies exhibiting the higher circulation. Although our measurements were performed in planes, asynchronously, our results strongly suggest the presence of elongated structures with their axis perpendicular to the primary jet flow, crossing the jet symmetry plane and stretching on either side of it. No definitive conclusion could be drawn as to whether the eddy structures present in the impingement region systematically appear in counter-rotating vortex pairs. About 80 % of the detected vortical tubes are located in a layer no deeper than 10 % of the nozzle-to-wall distance, and most of them are concentrated close to the impingement plate, in a region no deeper than 3 % of the nozzle-to-wall distance. They are evenly distributed spanwise. Our results suggest that the coherent structures present in the wall region of our jet are most likely due to the strong streamline curvature imposed by the presence of the impingement plate. However, further experiments, including time resolved measurements, would be required to state definitively that none of these structures comes from the upstream flow. In the jet central plane, they seem to be flattened out. This could perhaps be due to recompression of the main stream as it approaches the wall. As they are entrained by the lateral wall jets developing on either side of the main flow after impingement, the eddies grow in size and circulation. They also tend to lose their initial alignment with the normal to the jet plane.

Additional experiments have been performed on various air curtain arrangements. Their ongoing analysis, the results of which will form the subject of a future paper, seem to indicate that the topological features of the structures detected in the impingement region of the corresponding jets are primarily a function of the opening ratio H/e, which sets the shape of the streamlines in the impingement region. These characteristics do not depend on the initial flow conditions. Therefore, it seems possible to act passively on the flow in the impingement region to achieve tighter air curtains without questioning current methods of technical dimensioning. However, the energetic features of the eddy structures present in the impingement region seem to be fixed by the jet Reynolds number $U_0 e/\nu$. Thus, the main features of the coherent structures present in the disturbed wall region of a plane impinging jet are determined simultaneously by local and global characteristics of the main flow. These results, which are qualitatively consistent with those of Agrawal and Prasad (2002a), further raise the question of the choice of appropriate scales to normalize the results presented in this paper.

References

Adrian RJ, Christensen KT, Liu ZC (2000) Analysis and interpretation of instantaneous turbulent velocity fields. Exp Fluids 29: 275-290

Agrawal A, Prasad AK (2002a) Properties of vortices in the self-similar turbulent jet. Exp Fluids 33: 565-577

Agrawal A, Prasad AK (2002b) Organizational modes of large-scale vortices in an axisymmetric turbulent jet. Flow, Turb. Combust 68: 359-377

Agrawal A, Prasad AK (2003) Measurements within vortex cores in a turbulent jet. J Fluids Eng 125: 561-568

Antonia RA, Satyaprakash BR, Hussain AKMF (1980) Measurements of dissipation rate and some other characteristics of turbulent plane and circular jets. Phys. Fluids 23(4): 695-700

Beaubert F (2002) Simulation des grandes échelles turbulentes d'un jet plan en impact. PhD Report N°ED 0367-042, Université de Nantes.

Beaubert F, Viazzo S (2003) Large eddy simulation of plane turbulent impinging jets at moderate Reynolds numbers. Int J. Heat and Fluid flow 24: 512-519

Bonnet JP, Delville J, Glausner MN, Antonia RA, Bisset DK, Cole DR, Fiedler HE, Garem JH, Hilberg D, Jeong J, Kevlahan NKR, Ukeiley LS, Vincendeau E (1998) Collaborative testing of eddy structure identification methods in free turbulent shear flows. Exp Fluids 25:197-225

Bonnet JP, Delville J (2002) Coherent structures in turbulent flows and numerical simulations approaches. Von Karman Institute for Fluid Dynamics Lecture Series 2002-04 on Post-processing of experimental and numerical data, April 22-26

Chassaing P (2000) Turbulence en mécanique des fluides : Analyse du phénomène en vue de sa modélisation à l'usage de l'ingénieur. Collection Polytech INP Toulouse-Cépaduès Editions

Geers LFG, Tummers MJ, Hanjalic K (2005) Particle imaging velocimetry-based identification of coherent structures in normally impinging multiple jets. Phys. Fluids 17, 055105, 1-13.

Gupta S (2005) Etude expérimentale du comportement dynamique et des performances de rideaux d'air en vue de la conception de systèmes de confinement cellulaires, PhD Report N°ED 0367-174, Université de Nantes.

Hsiao FB, Huang JM (1994) On the dynamics of flow structure development in an excited plane jet. Trans. ASME 116: 714-720

Hussain F (1986) Coherent structures and turbulence. J Fluid Mech 173:303-356

Jeong J, Hussain F (1995) On the identification of a vortex. J Fluid Mech. 285:69-94

Lesieur M (1990) Turbulence in fluids. Kluwer editions.

Lyell MJ, Huerre P (1985) Linear and nonlinear stability of plane stagnation flow. J. Fluid Mech. 161: 295-312

Maurel S, Solliec C (2001) A turbulent plane jet impinging nearby and far from a flat plate. Exp. Fluids 31: 687-696

Maurel S, Rey C, Solliec C, Pavageau M (2004) Caractéristiques structurelles d'un jet d'air plan turbulent frappant une plaque plane placée à distance variable. Mécanique & Industries 5: 317-329

Najjar FM, Tafti DK (1996) Study of discrete test filters and numerical approximations for the dynamic subgrid-scale stress model in turbulent channel flow simulations. Phys Fluids 8(4): 1076-1088

Rajagopalan S, Ko NWM (1996) Velocity and spanwise vorticity measurements in an excited mixing layer of a plane jet. Exp Fluids 20: 346-357

Rajagopalan S, Antonia RA (1998) Turbulence reduction in the mixing layer of a plane jet using small cylinders. Exp Fluids 25: 86-103

Robinson SK (1991) Coherent motion in the turbulent boundary layer. Ann Rev Fluid Mech 23: 601-639

Robinson SK, Kline SJ, Spalart PR (1989) Quasi-coherent structures in the turbulent boundary layer. Part II: verification and new information from a numerically simulated flat-plate boundary layer. In: Kline SJ, Afgan NH (ed) Near wall turbulence. Proceedings of Zaric Memorial Conference, New York Hemisphere: 218-247

Sakakibara J, Hishida K, Maeda M (1997) Vortex structure and heat transfer in the stagnation region of an impinging plane jet (simultaneous measurements of velocity and temperature fields by digital particle image velocimetry and laser-induced fluorescence). Int. J. Heat Mass Transfer 40(13): 3163-3176

Schram C, Rambaud P, Riethmuller ML (2004) Wavelet based eddy structure eduction from a backward facing step flow investigated using PIV. Exp Fluids 36: 233-245

Vandsburger U, Ding C (1995) Self-excited wire method for the control of turbulent mixing layers, AIAA J. 33(6): 1032-1037

Yokobori S, Kasagi N, Hirata M (1977) Characteristic behaviour of turbulence in the stagnation region of a two-dimensional submerged jet impinging normally on a flat plate. Proc. of Symposium on Turbulent Shear Flows, April 18-20, Pennsylvania: 3.17-3.25

Zaman KBMQ, Hussain AKMF (1981) Turbulence suppression in free shear flows by controlled excitation. J. Fluid Mech. 103: 133-159

Acknowledgements

The work presented in this paper was supported by the CNRS, the EMN and the French Embassy in New-Delhi (India) in the form of Post-doctoral and PhD grants. It could not have been completed without the assistance of the technical staff of our laboratory. We thank, in particular, Mr. Y. Gouriou, Mr. F.X. Blanchet and Mr. E. Chevrel for their valuable and unstinting help in the construction and instrumentation of the experimental facility designed for this work.

LIST OF TABLES

FIGURE CAPTIONS

Figure 1 Effect of Galilean transformation with a uniform translational velocity

- **(a)** Velocity field viewed in a reference frame moving at the velocity of the centre of a Taylor Green vortex transported by a uniform flow
- **(b)** Velocity field viewed in a reference frame moving at the velocity of the centre of a Taylor Green vortex transported by a pure shear flow

Figure 2 Schematic view of the experimental apparatus

Figure 3 Mean flow characteristics in the xy-plane at the tunnel centre plane

- **(a)** Mean velocity field $\overline{U}/U_0$ (one vector out of two has been skipped in both directions for clarity)
- **(b)** Streamlines
- **(c)** rms of the x-component of velocity σ_U/U_0
- **(d)** rms of the y-component of velocity σ_V/U_0
- **(e)** Reynolds stress $\overline{u'v'}/U_0^2$
- **(f)** Turbulent kinetic energy $\left(\sigma_U^2+\sigma_V^2\right)/U_0^2$

Figure 4 Position of the five measurement planes

Figure 5 Mean flow characteristics in xz-planes

- **(a)** Normalised mean velocity magnitude at *y/ e*= -3
- **(b)** Normalised mean velocity magnitude at *y/e* = -1
- **(c)** Normalised mean velocity magnitude at *y/e* = 0
- **(d)** Normalised mean velocity magnitude at *y/e* = 1
- **(e)** Normalised mean velocity magnitude at *y/e* = 3
- **(f)** Normalised mean velocity divergence at *y/e* = 0

Figure 6 Distribution of turbulent kinetic energy attenuation in wave number space after application of a filter of width 7 × 7 grid points (xz-plane *y/e* = 0)

Figure 7 Comparison of present and Schram et al. (2004) λ_2-threshold methods

Figure 8 In the five measurement planes:

- **(a)** Proportion of closed and open structures
- **(b)** Mean of the pdf of normalised mean diameter (closed structures only)
- **(c)** Mean of the pdf of normalised mean diameter along the 4 directions (closed structures only)
- **(d)** Mean of the pdf of eccentricity (closed structures only)
- **(e)** Proportion of anticlockwise and clockwise rotating vortices
- **(f)** Mean of the pdf of normalised vortical intensity (closed structures only)

Figure 9 Probability density functions of mean diameter of closed structures

Figure 10 Distribution of closed structures with respect to the orientation of their maximal / minimal diameter versus eccentricity ranges (xz-plane $y/e = 0$)

Figure 11

- **(a)** Two-dimensional probability distribution of presence of detected vortices in the xz-plane $y/e = 0$
- **(b)** Cumulative histogram of density of presence of closed structures vs. distance from the impingement wall

Figure 12

- **(a)** Distribution of normalised circulation vs. mean diameter in the xz-plane $y/e = 0$
- **(b)** Probability density function of normalised circulation in the five measurement planes (CW rotating vortices only – in percent with respect to the total number of positive vortices)

Figure 13

- **(a)** Probability density function of normalised vortical intensity in the five measurement planes (in percent with respect to the total number of exposed vortices)
- **(b)** Distribution of normalised vortical intensity vs. mean diameter in the xz-plane $y/e = 0$

Field of view (mm^2)	61.6×62.1 ($\approx 2e \times 2e$)
Interrogation area size ($pixels^2$)	16 x 16
Interrogation area size (mm^2)	0.978×0.978 ($\approx e/30 \times e/30$)
Interrogation area overlap in both directions	50 %
Spatial resolution of vector maps (mm)	0.489 ($\approx e/60$)
Number of vectors in vector maps	125×126
Camera focal length lens (mm)	28
Numerical aperture	4
Pulse delay (μs)	30
Dynamic velocity range (m/s)	0.030:7.9
Accuracy with a 95% confidence level	±1%
Average number of recorded pairs of images	≈ 450
Velocity-field filter size (grid points)	7 x 7 (σ = 0.65 times the filter box size)
λ_2-field filter size (grid points)	7 x 7 (σ = 0.65 times the filter box size)
$\lambda_{2,threshold}$	40 %

Table 1

Filter width (in grid points)	Attenuation calculated from instantaneous velocity fields (%)	Attenuation calculated from fluctuating velocity fields (%)
3 × 3	2	7
5 × 5	3	13
7 × 7	4	18
9 × 9	5	24
11 × 11	6	29

Table 2

Filter width (in grid points)	No filtering	3 × 3	5 × 5	9 × 9	13 × 13
Total number of detected structures	3432	2399	1829	1222	911
Proportion of closed structures (%)	53	59	64	69	75
Proportion of structures with one open direction (%)	33	30	27	23	21
Average eccentricity	2.8	2.4	2.2	2.1	1.9
Median eccentricity	2.2	2.0	2.0	1.8	1.8
Standard deviation of eccentricity	2.15	1.97	1.01	0.79	0.59
Average mean diameter (mm)	7.2	7.7	8.1	8.6	9.4
Median mean diameter (mm)	7.2	7.8	8.1	8.6	9.8
Average mean diameter (grid points)	14.8	15.6	16.5	17.6	19.16
Standard deviation of average mean diameter (mm)	3.6	3.6	3.7	3.8	3.9

Table 3

λ_2-filter width (in grid points)	3 × 3	7 × 7	11 × 11
Total number of detected structures	1471	1080	866
Proportion of closed structures (%)	66	69	70
Proportion of structures with one open direction (%)	25	23	23
Average eccentricity	2.1	2.1	2.1
Median eccentricity	1.9	1.9	1.9
Average mean diameter (mm)	8.4	8.4	8.4
Median mean diameter (mm)	8.9	8.5	8.5

Table 4

Threshold value (%)	10	20	40	60
Total number of detected structures	2092	1080	426	240
Proportion of closed structures (%)	62	69	76	81
Proportion of structures with one open direction (%)	28	23	19	15
Average eccentricity	2.19	2.14	2.05	1.95
Median eccentricity	1.9	1.9	1.85	1.85
Average mean diameter (mm)	8.7	8.4	7.5	6.9
Median mean diameter (mm)	9.2	8.5	7.0	6.6

Table 5

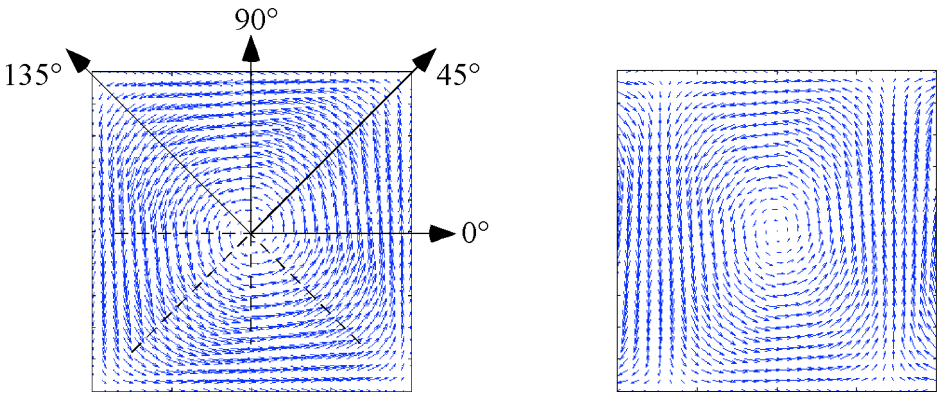

Figure 1

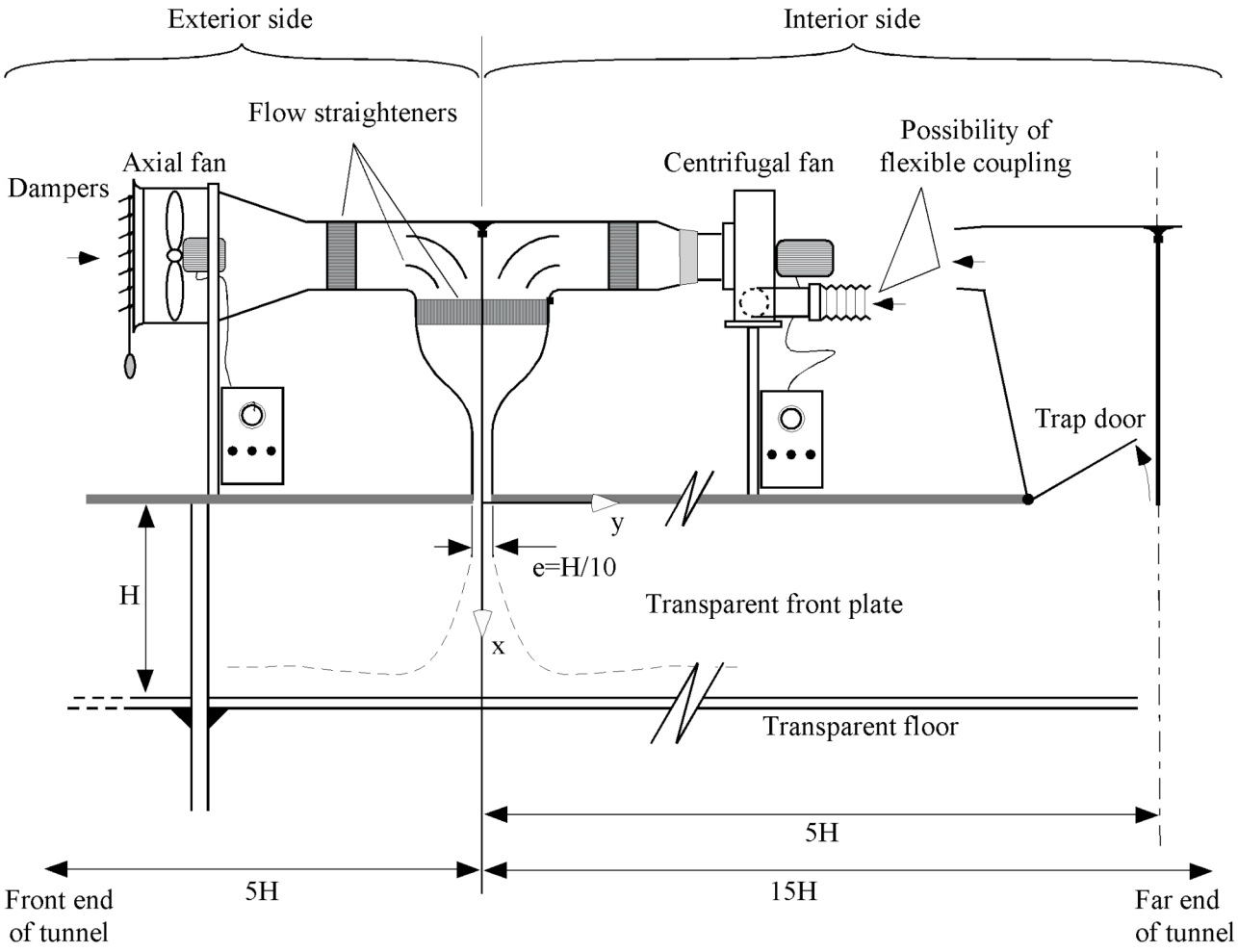
Exterior side
Interior side
Flow straighteners
Possibility of
flexible coupling
Axial fan
Dampers
Centrifugal fan
Trap door
y
e=H/10
H
Transparent front plate
x
Transparent floor
5H
5H
15H
Front end
of tunnel
Far end
of tunnel

Figure 2

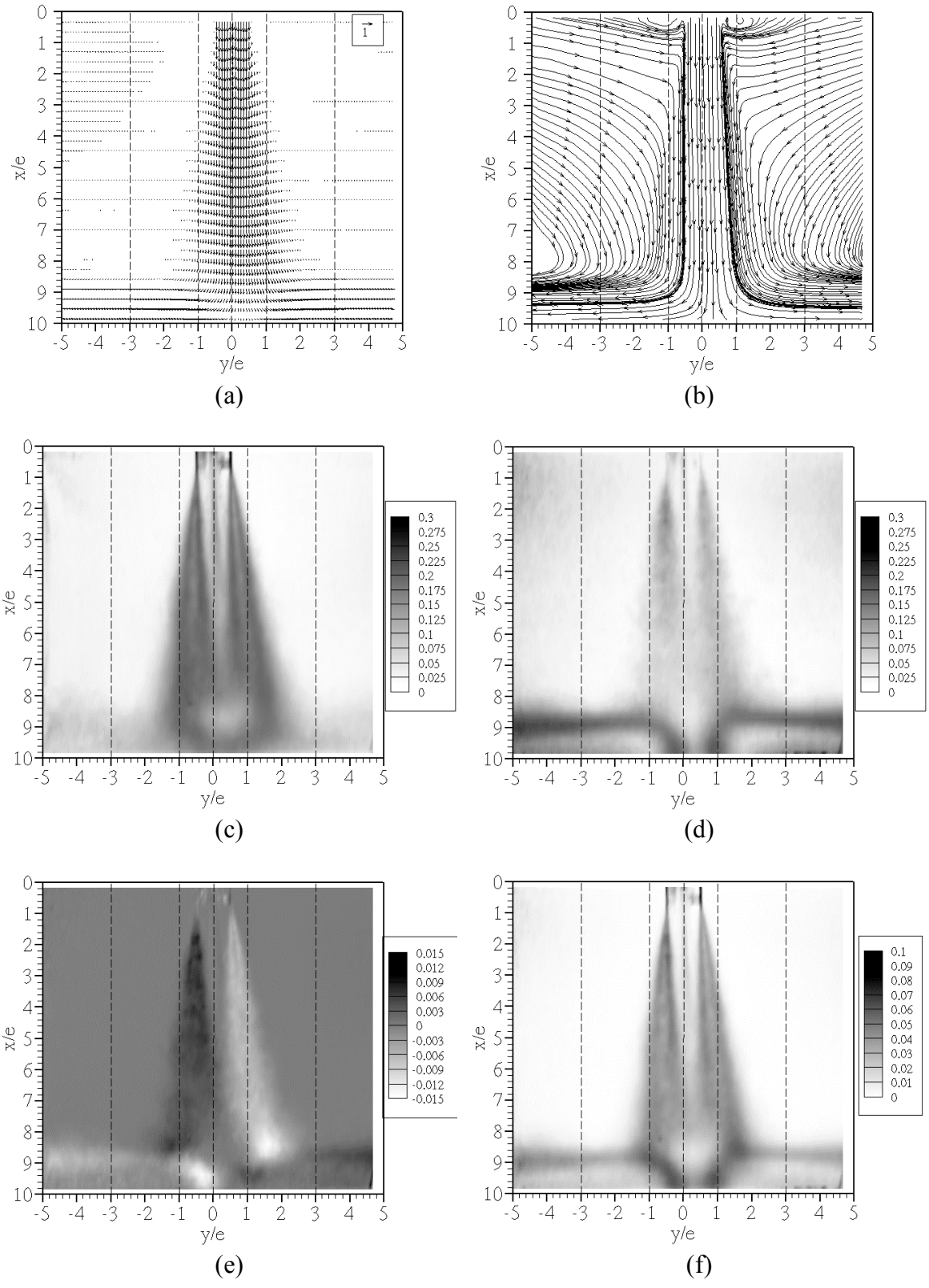
x/e
y/e
(a)
(b)
0.3
0.275
0.25
0.225
0.2
0.175
0.15
0.125
0.1
0.075
0.05
0.025
0
(c)
(d)
0.015
0.012
0.009
0.006
0.003
0
-0.003
-0.006
-0.009
-0.012
-0.015
0.1
0.09
0.08
0.07
0.06
0.05
0.04
0.03
0.02
0.01
(e)
(f)

Figure 3

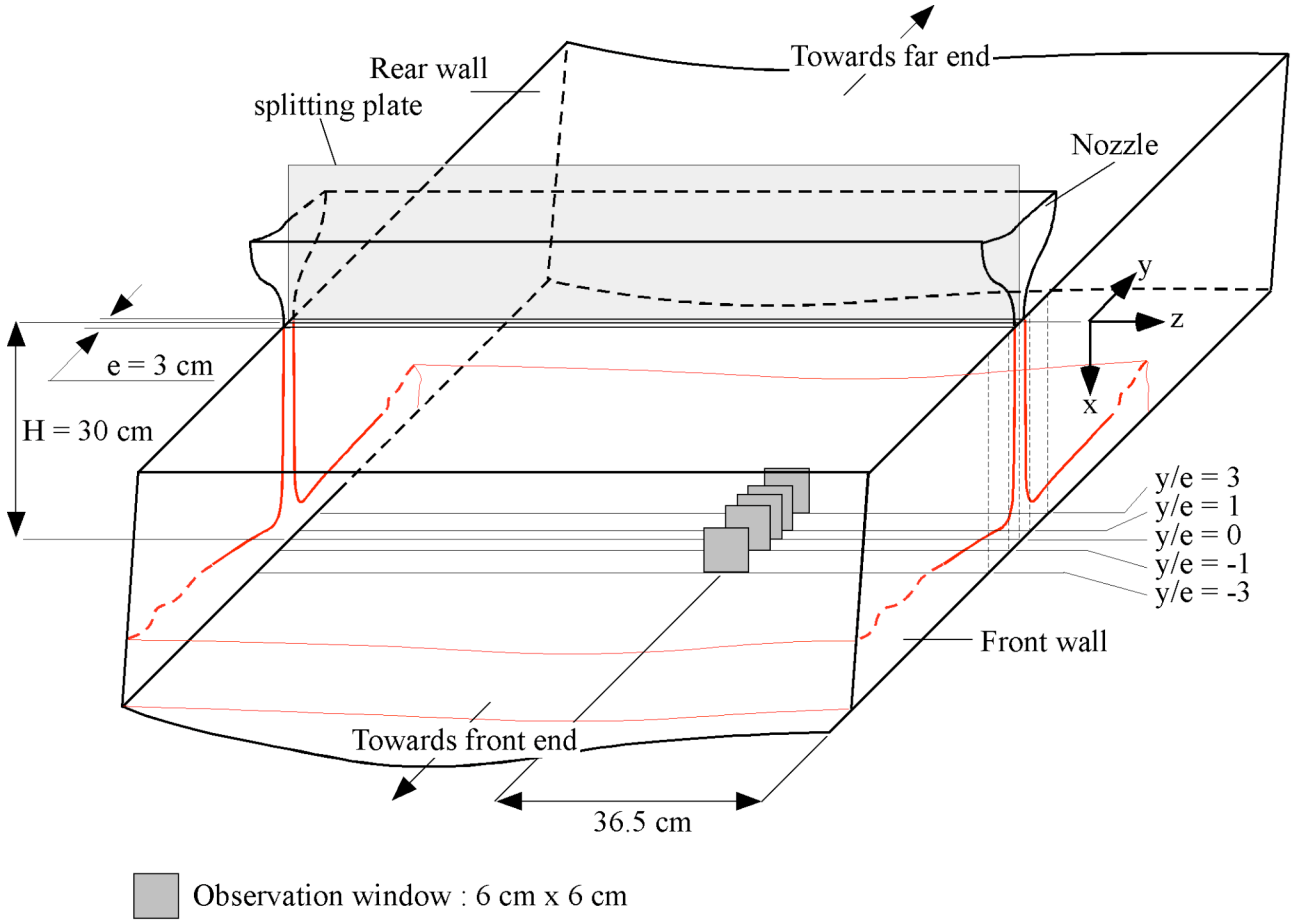
Towards far end
Rear wall
splitting plate
Nozzle
y
z
x
e = 3 cm
H = 30 cm
y/e = 3
y/e = 1
y/e = 0
y/e = -1
y/e = -3
Front wall
Towards front end
36.5 cm
Observation window : 6 cm x 6 cm

Figure 4

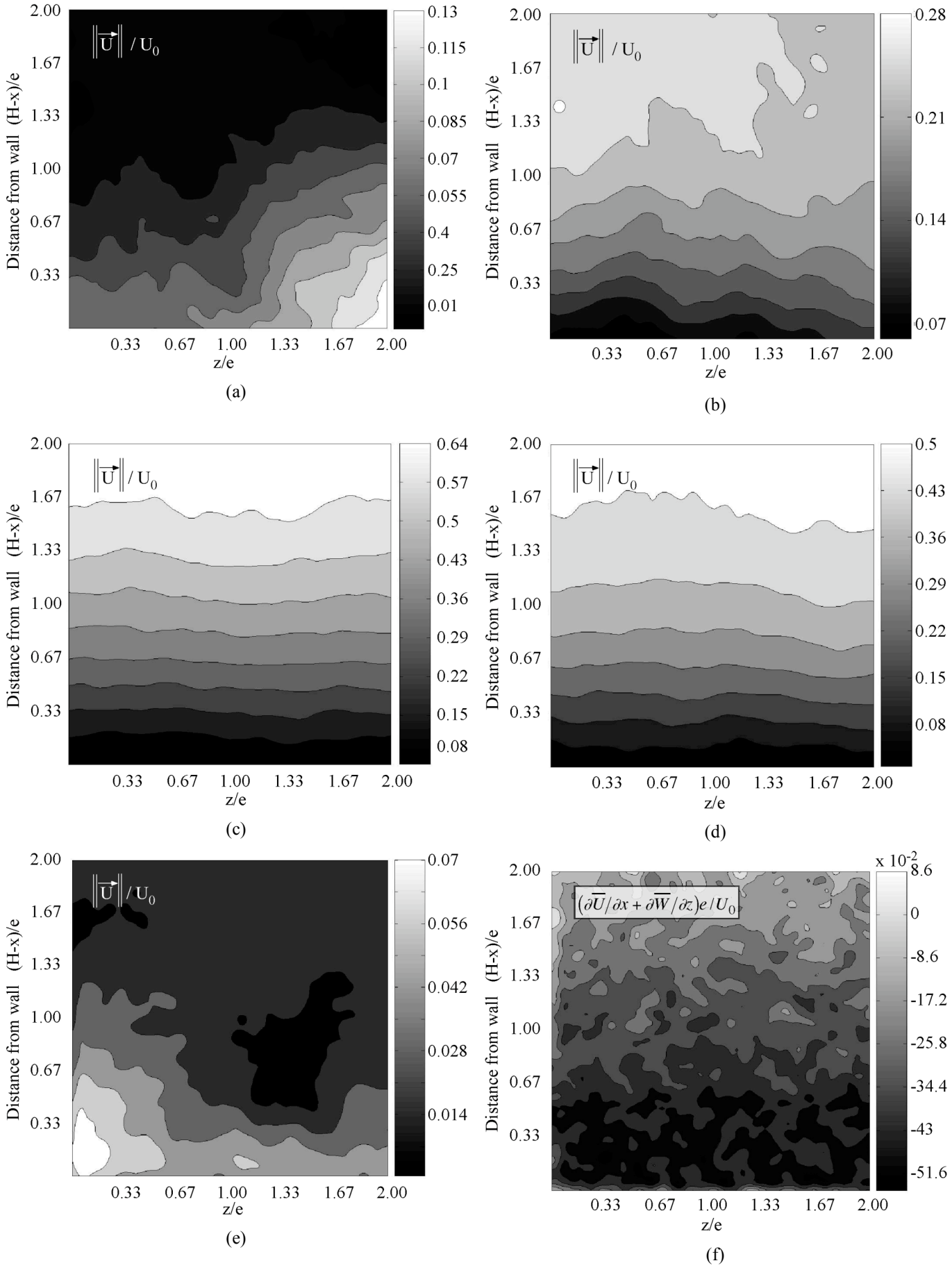
$\|\vec{U}\| / U_0$
Distance from wall (H-x)/e
z/e
2.00
1.67
1.33
1.00
0.67
0.33
(a)
0.13
0.115
0.1
0.085
0.07
0.055
0.4
0.25
0.01
(b)
0.28
0.21
0.14
0.07
(c)
0.64
0.57
0.5
0.43
0.36
0.29
0.22
0.15
0.08
(d)
0.5
0.43
0.36
0.29
0.22
0.15
0.08
(e)
0.07
0.056
0.042
0.028
0.014
(f)
$(\partial\overline{U}/\partial x + \partial\overline{W}/\partial z)e/U_0$
x 10^{-2}
8.6
0
-8.6
-17.2
-25.8
-34.4
-43
-51.6

Figure 5

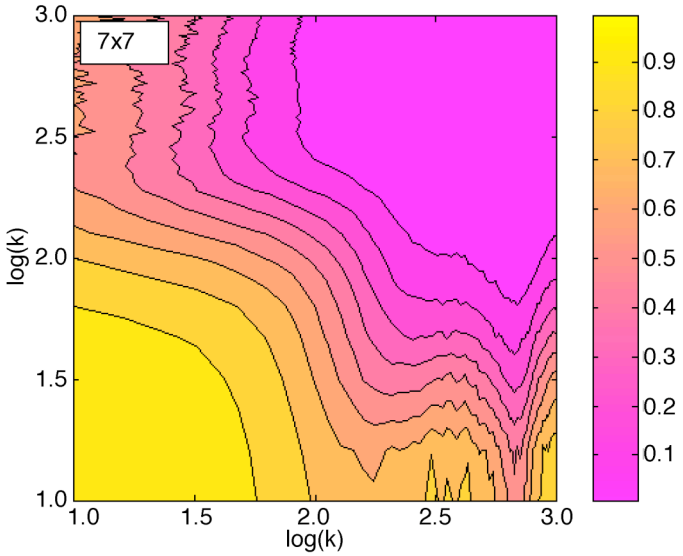

Figure 6

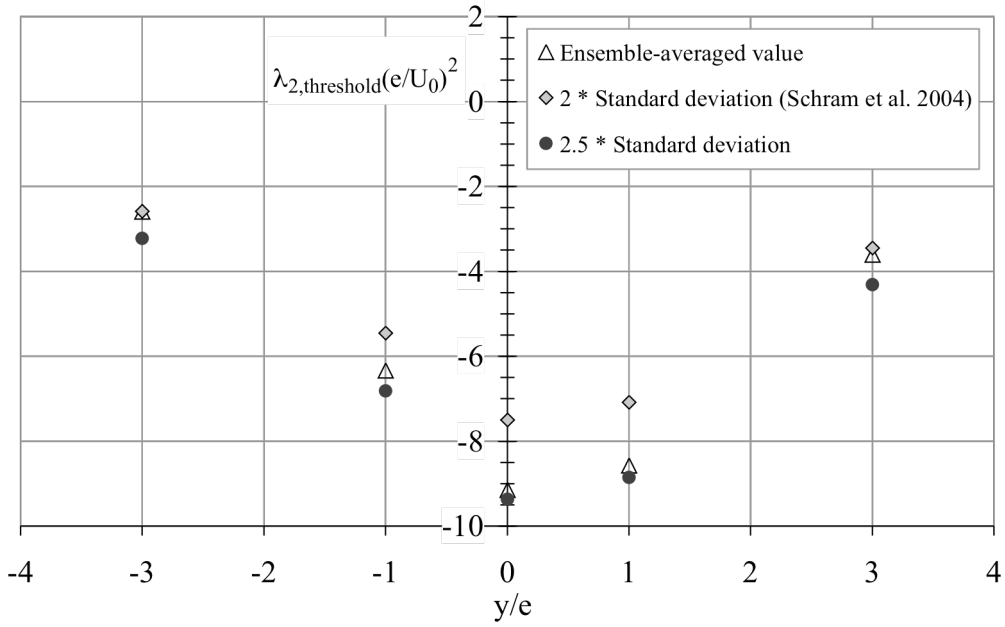
$\lambda_{2,threshold}(e/U_0)^2$
△ Ensemble-averaged value
◇ 2 * Standard deviation (Schram et al. 2004)
● 2.5 * Standard deviation
2
0
-2
-4
-6
-8
-10
-4
-3
-2
-1
0
1
2
3
4
y/e

Figure 7

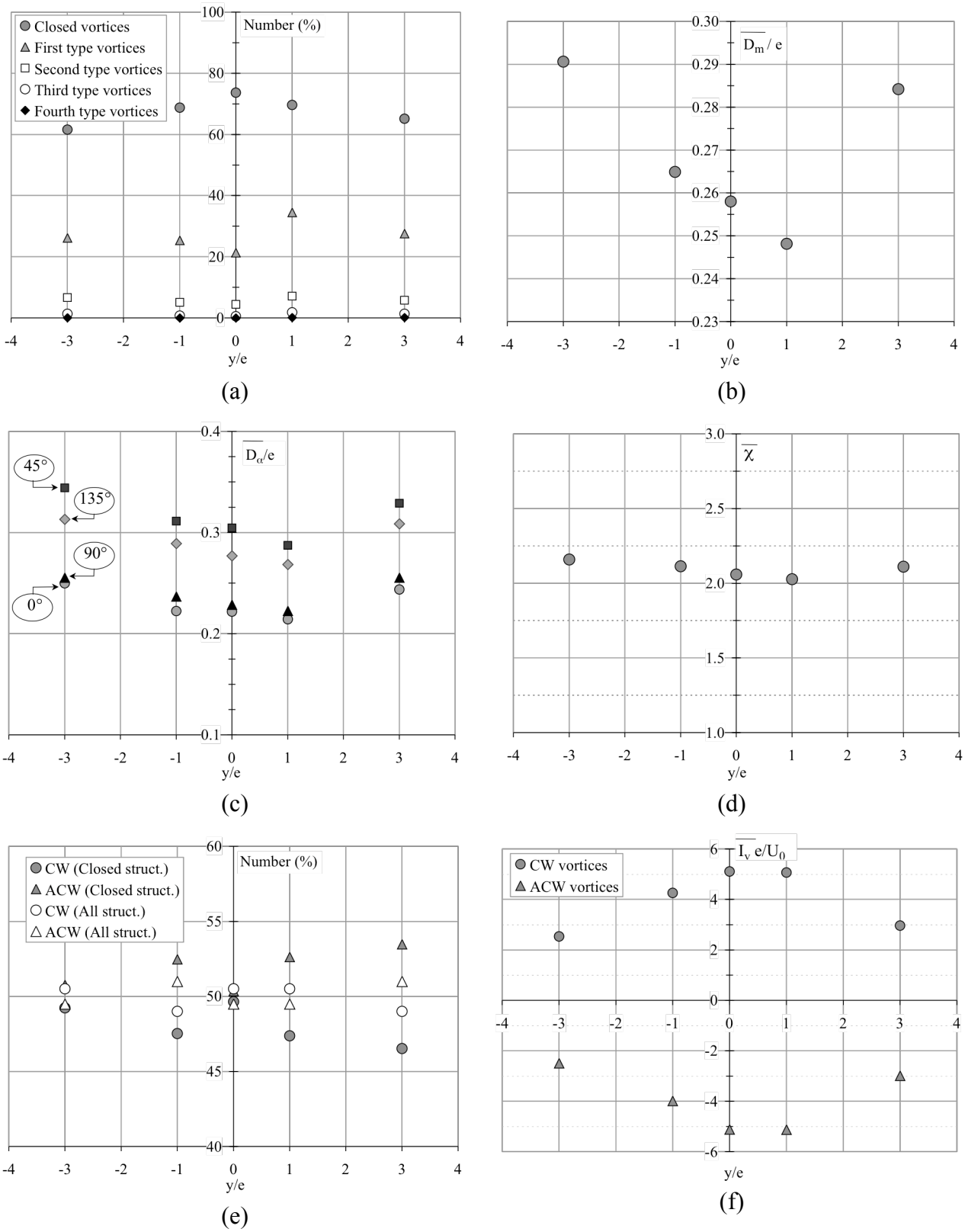
Closed vortices
First type vortices
Second type vortices
Third type vortices
Fourth type vortices
Number (%)
y/e
(a)
$\overline{D_m}$ / e
y/e
(b)
45°
135°
90°
0°
$\overline{D_\alpha}$/e
y/e
(c)
$\overline{\chi}$
y/e
(d)
CW (Closed struct.)
ACW (Closed struct.)
CW (All struct.)
ACW (All struct.)
Number (%)
y/e
(e)
CW vortices
ACW vortices
$\overline{I_v}$ e/U$_0$
y/e
(f)

Figure 8

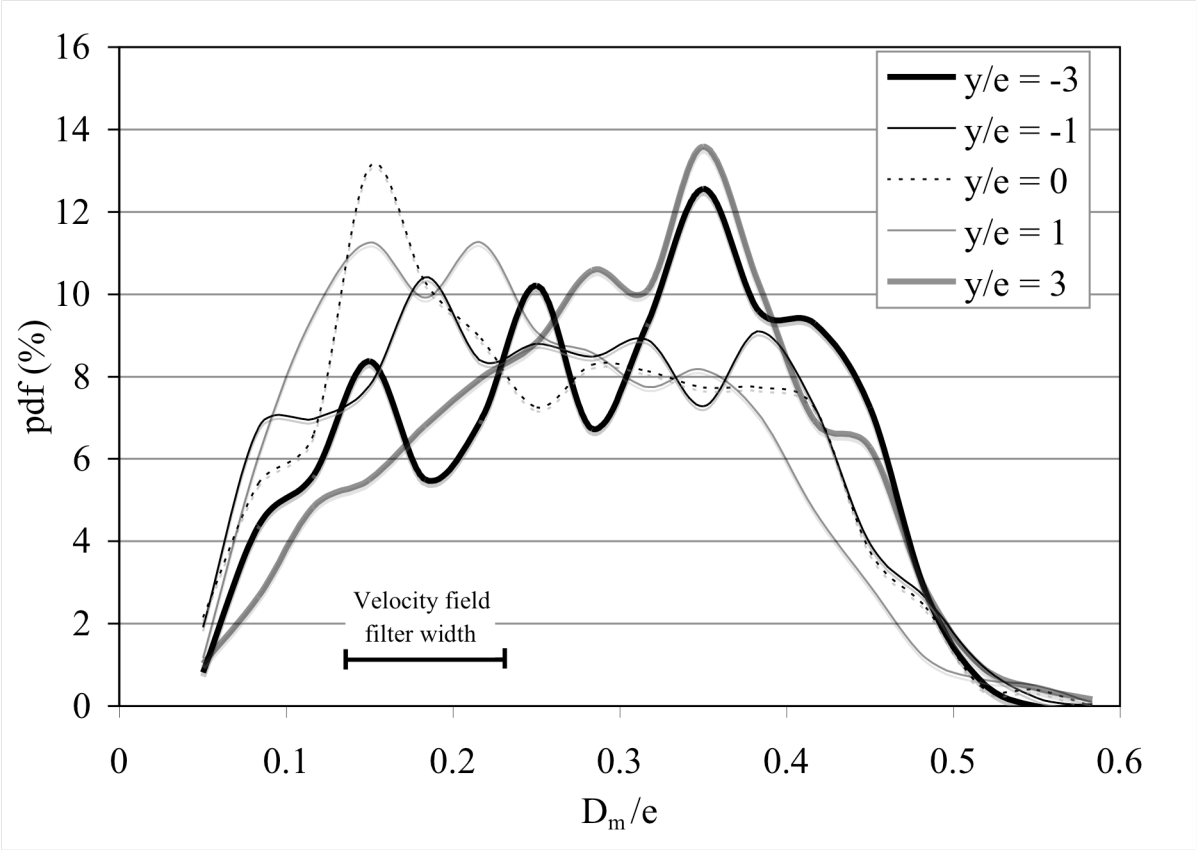
16
14
12
10
8
6
4
2
0
pdf (%)
0
0.1
0.2
0.3
0.4
0.5
0.6
D_m/e
y/e = -3
y/e = -1
y/e = 0
y/e = 1
y/e = 3
Velocity field
filter width

Figure 9

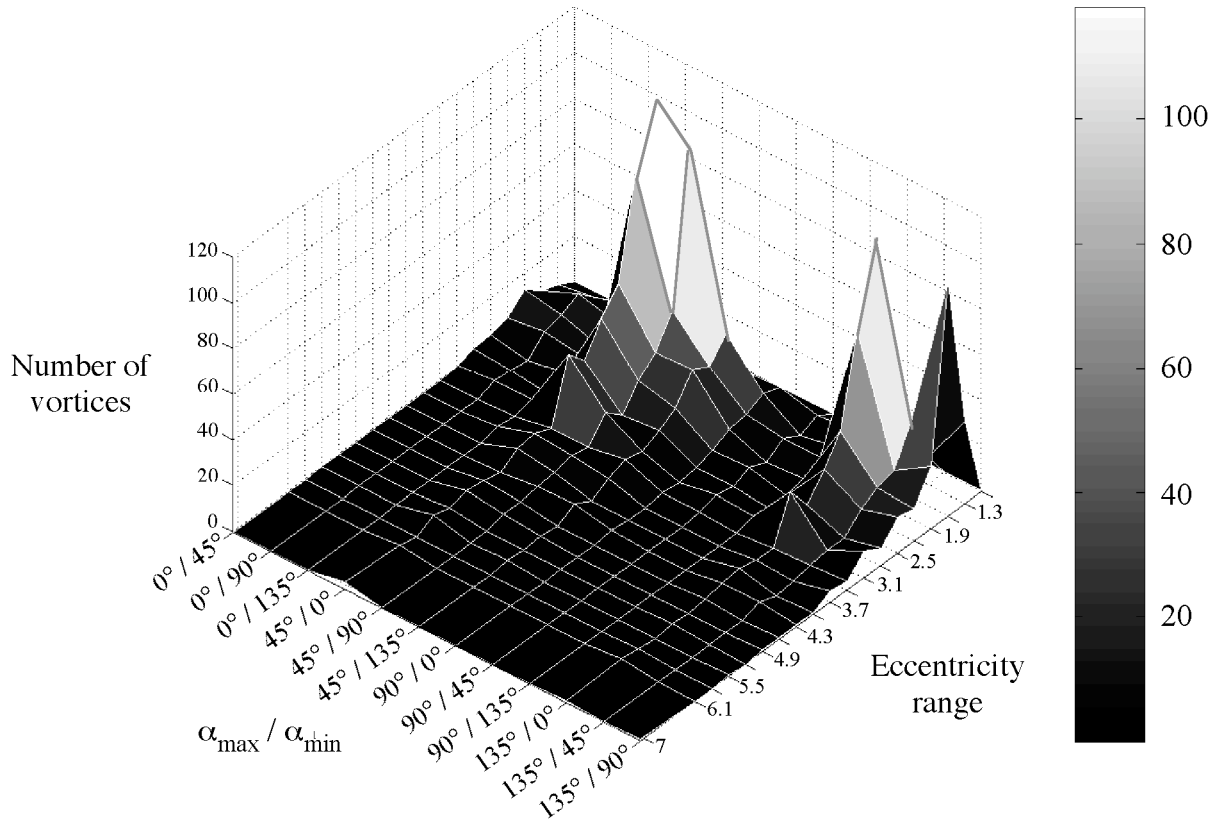
Number of vortices
120
100
80
60
40
20
0
0° / 45°
0° / 90°
0° / 135°
45° / 0°
45° / 90°
45° / 135°
90° / 0°
90° / 45°
90° / 135°
135° / 0°
135° / 45°
135° / 90°
αmax / αmin
1.3
1.9
2.5
3.1
3.7
4.3
4.9
5.5
6.1
7
Eccentricity range
100
80
60
40
20

Figure 10

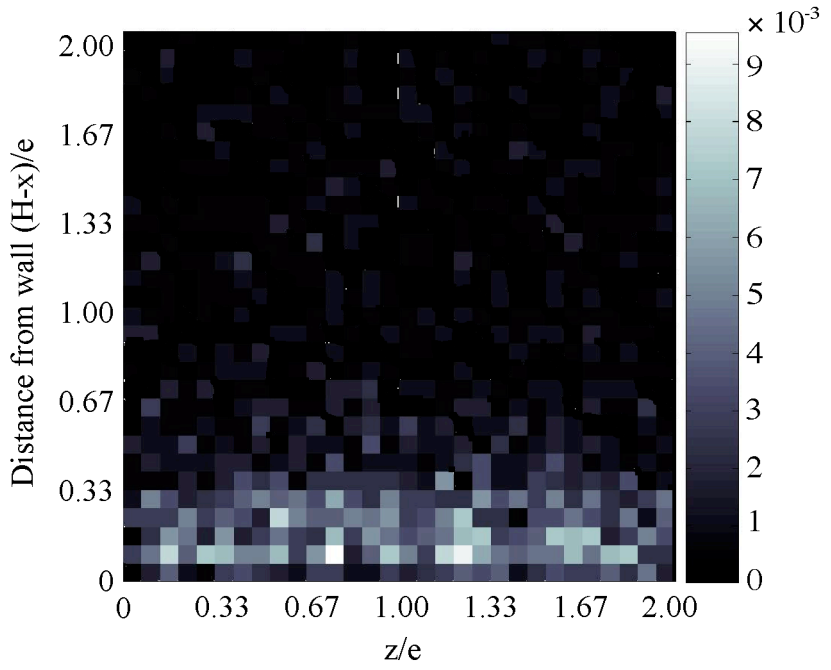
× 10-3
9
8
7
6
5
4
3
2
1
0
2.00
1.67
1.33
1.00
0.67
0.33
0
Distance from wall (H-x)/e
0
0.33
0.67
1.00
1.33
1.67
2.00
z/e

(a)

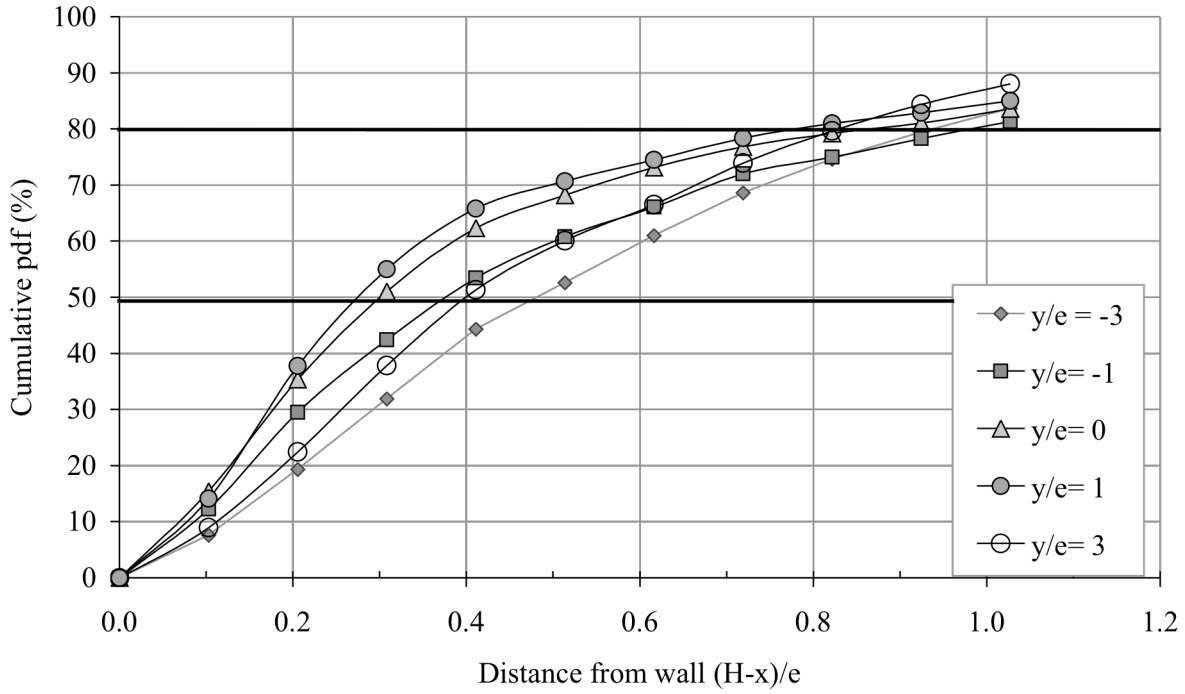
100
90
80
70
60
50
40
30
20
10
0
Cumulative pdf (%)
0.0
0.2
0.4
0.6
0.8
1.0
1.2
Distance from wall (H-x)/e
y/e = -3
y/e= -1
y/e= 0
y/e= 1
y/e= 3

(b)

Figure 11

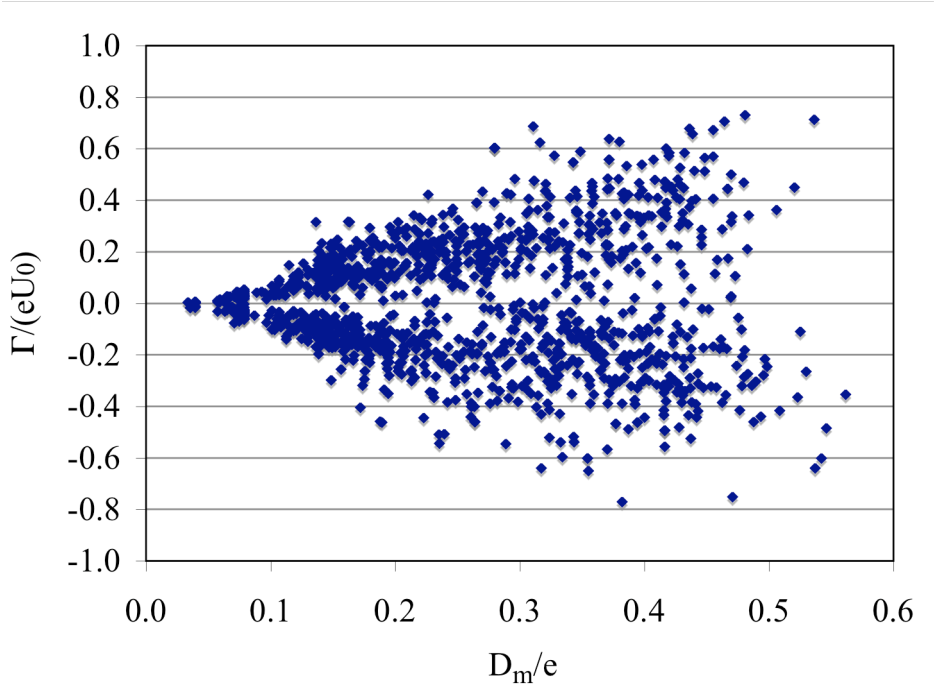
1.0
0.8
0.6
0.4
0.2
0.0
-0.2
-0.4
-0.6
-0.8
-1.0
Γ/(eU0)
0.0
0.1
0.2
0.3
0.4
0.5
0.6
Dm/e

(a)

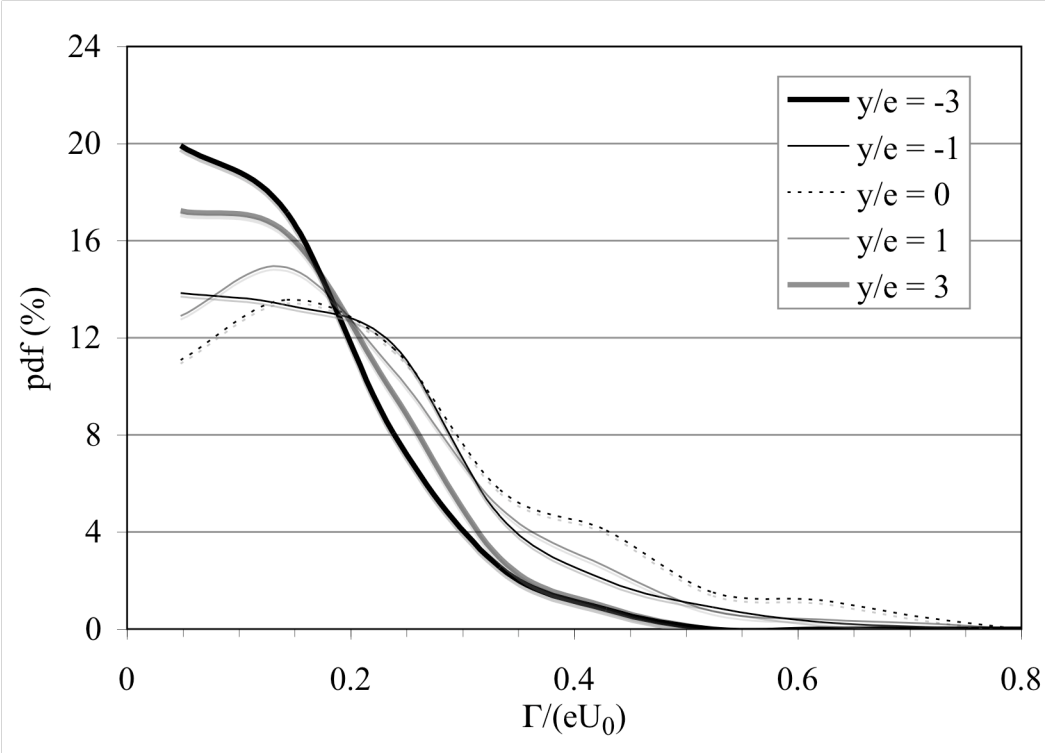
24
20
16
12
8
4
0
pdf (%)
0
0.2
0.4
0.6
0.8
Γ/(eU0)
y/e = -3
y/e = -1
y/e = 0
y/e = 1
y/e = 3

(b)

Figure 12

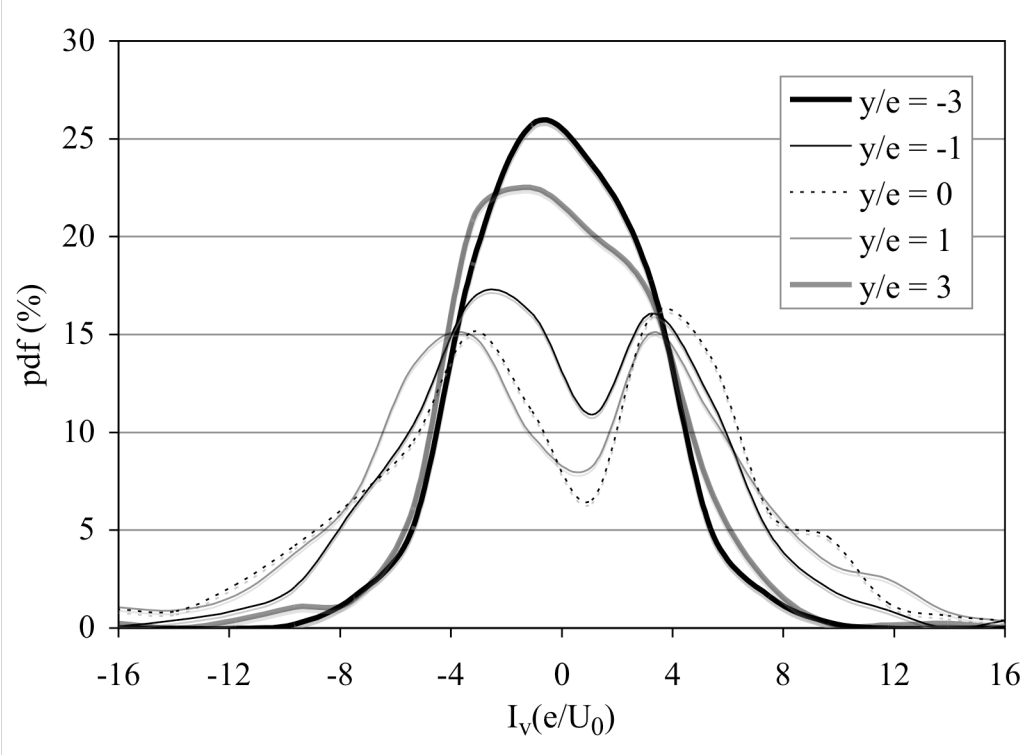
30
25
20
15
10
5
0
pdf (%)
-16
-12
-8
-4
0
4
8
12
16
$I_v(e/U_0)$
y/e = -3
y/e = -1
y/e = 0
y/e = 1
y/e = 3

(a)

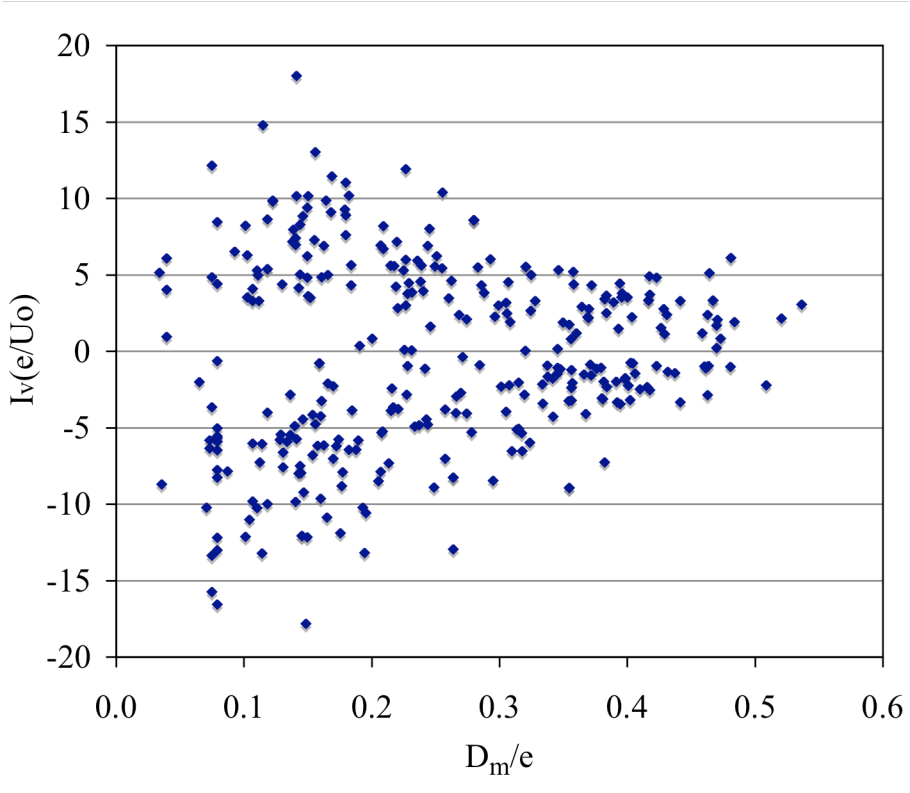
20
15
10
5
0
-5
-10
-15
-20
$I_v(e/U_o)$
0.0
0.1
0.2
0.3
0.4
0.5
0.6
D_m/e

(b)

Figure 13